



1 Mechanical compaction mechanisms in the input sediments of the
2 Sumatra Subduction Complex- insights from microstructural analysis of
3 cores from IODP Expedition- 362

4 Sivaji Lahiri^{1*}, Kitty L. Milliken², Peter Vrolijk³, Guillaume Desbois¹, Janos L. Urai¹

5 ¹Institute of Tectonics and Geodynamics, RWTH Aachen University, Germany, Lochnerstrasse 4–20, 52056,
6 Aachen, Germany

7 ²Bureau of Economic Geology, The University of Texas at Austin, Austin, TX, 10611, USA

8 ³Applied Ocean Science and Engineering, Woods Hole Oceanographic Institution, Woods Hole, MA, United
9 States

10 * Corresponding author: sivaji.lahiri2@gmail.com

11

12 Abstract

13 The input sediments of the North Sumatra subduction zone margin, drilled during IODP Expedition 362, exhibit
14 remarkable uniformity in composition and grain size over the entire thickness of the rapidly deposited Nicobar
15 Fan succession (sea-floor to 1500 mbsf depth), providing a unique opportunity to study the micromechanisms of
16 compaction. Samples were prepared from dried core samples from sites (U1480 and U1481) by both Ar-ion cross-
17 section polishing and broad-ion beam cutting, and imaged with a field-emission SEM. Shallowest samples (sea-
18 floor to 28mbsf) display a sharp reduction in porosity from 80% to 52% due to collapse of large clay-
19 domain/matrix pores associated with rotation and realignment of clay-platelets parallel to the bedding plane. The
20 deeper succession (28mbsf to 1500mbsf) exhibits less rapid reduction in porosity from 52% to 30% by the
21 progressive collapse of silt-adjacent larger pores by bending and subsequent sliding/fracturing of clay particles. In
22 addition, there is a correlated loss of porosity in the pores too small to be resolved by SEM.

23 Clastic particles show no evidence of deformation or fracturing with increasing compaction. In the phyllosilicates,
24 there is no evidence for pressure solution or recrystallization: thus, compaction proceeds by micromechanical
25 processes. Increase in effective stress up to 18 MPa (~1500mbsf) causes the development of a weakly aligned
26 phyllosilicate fabric defined by illite clay particles and mica grains, while the roundness of interparticle pores
27 decreases as the pores become more elongated. We propose that bending of the phyllosilicates by intracrystalline
28 slip may be the rate-controlling mechanism.

29 Pore size distributions show that all pores within the compactional force chain deform, irrespective of size, with
30 increasing compactional strain. This arises because the force chain driving pore collapse is localized primarily



31 within the volumetrically dominant and weaker clay-rich domains; pores associated with packing around isolated
32 silt particles enter into the force chain asynchronously and do not contribute preferentially to pore loss over the
33 depth range studied.

34 Introduction

35 Muds are fine-grained sediments (>50% of particles <63µm diameter) comprising platy detrital clay minerals and
36 equidimensional detrital grains such as quartz, feldspar, calcite, etc. (Nakano, 1967; Hesse, R., 1975; Sintubin,
37 1994). Understanding the mechanical, chemical, and microstructural properties of mud and mudstone is of great
38 interest for rock property prediction in basic earth science, in exploration, subsurface integrity studies and
39 geotechnical engineering (Yagiz, S., 2001; Aplin and Yagiz, 2011; Lazar et al., 2015). The chemical and physical
40 behavior of marine muds plays a critical role in defining the geometry of accretionary prisms, locating the
41 décollement for fault rupture (Vrolijk, 1990; Chester et al., 2013) and understanding subduction zone earthquakes
42 and tsunamis (Dean et al., 2010; Chester et al., 2013; Hüpers et al., 2017).

43 Marine mud is deposited with a highly porous isotropic fabric (Bowles, 1969; Bennett et al. 1981; Bennett et al.
44 1991); depositional porosity in mud is about twice as high as in sand (e.g., Velde, 1996, Lundegard, 1992). In
45 contrast, mudstones have low porosities, modal pore sizes measured in nm, and an absence of textural controls on
46 porosity (e.g. Aplin et al., 2006; Milliken et al., 2012; Milliken et al., 2013). The processes in this dramatic
47 evolution of porosity has similarities to compaction of sand to sandstone, comprising a combination of compaction
48 and cementation (Milliken and Day-Stirrat, 2013), although the much smaller, elongated phyllosilicate grains
49 increase the role of clay-bound water in the process (Karaborni et al., 1996). Whereas a refined and somewhat
50 predictive understanding exists for porosity evolution in sand and sandstones (e.g., Lander and Walderhaug, 1999;
51 Paxton et al., 2002; Lander et al., 2008; Adjukiewicz and Lander, 2010, Desbois et al., 2011), such a model is at
52 best preliminary for muds and mudstones (Pommer and Milliken, 2015; Milliken and Olson, 2017). It seems clear
53 that the composition of the grain assemblage importantly sets the stage for porosity evolution in muds (Milliken,
54 2014), cementation being the greatest in muds with abundant biogenic debris. In contrast to sandstones, however,
55 cementation is far less common globally in mudstones (Milliken, 2019), leading to the notion that mechanical
56 compaction may be far more important in muds. Establishing the expected compaction behavior for muds in a
57 setting of well-constrained mud properties is an essential contribution that our study hopes to serve.

58 Investigations of mud and mudstone compaction are usually based on proxy data, such as velocity or density,
59 rather than direct measurements of porosity (e.g., references in Mondol, 2007). Direct measurement of porosity
60 can be broadly classified into two categories: 1) laboratory experiments; (e.g., Mitchell, 1956; Bennett et al. 1981;
61 Vasseur et al. 1995; Mondol et al. 2007; Fawad et al. 2010; Emmanel and Day-Stirrat, 2012), and 2) studies on
62 natural samples (e.g., Meade, 1964; Ho et al., 1999; Aplin et al. 2003, 2006; Day-Stirrat et al., 2008; 2010; 2012;
63 Milliken et al, 2012, Milliken et al., 2013). A common shortcoming of studies on natural samples is the assumption
64 that the bulk porosity is a direct measure of compaction although porosity loss has contributions of both
65 compaction and cementation (Lundegard, 1992; Ehrenberg, 1989; Paxton et al., 2002), and this can only be
66 accomplished by petrographic inspection (Milliken and Curtis, 2017). Experimental studies generally avoid this
67 shortcoming by the use of lab-produced particle packs that undergo no chemical change during the experiment.



68 Studies of shallowly buried units (like the present study) are the ones most likely to avoid the complication of
69 cementation, especially if temperatures are low and bulk grain assemblages are siliciclastic (Milliken, 2014).

70 Previous studies report contrasting ideas about the mechanisms of mechanical compaction of mud. According to
71 some studies, burial compaction significantly increases the alignment of phyllosilicate (clay and mica) parallel to
72 the bedding planes (Bowles et al., 1969; Oertel and Curtis, 1972; Vasseur et al., 1995). Other studies state that
73 intense mechanical compaction has a limited impact on the development of phyllosilicate fabric in mud (Ho et al.,
74 1999; Aplin et al., 2006; Day-Stirrat et al., 2008; 2011). These studies investigated the changes in particle
75 alignment and reduction in porosity (Ho et al., 1999; Aplin et al., 2006; Day-Stirrat et al., 2008; 2011) but without
76 imaging the evolution of pore morphology with increasing compactional strain. This is where this study aims
77 contribute.

78 We received 55 mud samples from drill cores collected during IODP Expedition 362 west of the North Sumatra
79 subduction zone margin and investigated the evolution of petrographic microstructure and pore morphology as a
80 function of compactional strain. Apart from general implications for global mudrocks, we hope this investigation
81 will also contribute to studies that seek to predict rock properties in the deeper subsurface at the Sumatra
82 subduction front.

83

84 Geological background and drilling

85 The Sumatra subduction zone extends 5000km from the Andaman-Nicobar Islands in the northwest to the Java-
86 Banda arc in the Southeast (Fig.1a and b) (Prawirodirdjo et al., 1997; Hippchen and Hyndman, 2008). The trench
87 of the Sumatra subduction zone (Fig.1a) developed on the subducting Indo-Australian Plate at a convergence rate
88 of 5.5 cm/yr in the north and 7.23 cm/yr in the South (Ghosal et al., 2014; Moeremans, and Singh, 2015).

89 On 26th December 2004, the west coast of Northern Sumatra recorded one of the largest earthquakes (Mw-9.3) in
90 the 21st century, generating a devastating Tsunami in the Indian Ocean (Ammon et al., 2005; Lay et al., 2005).
91 Understanding the mechanism(s) behind this unprecedented event was the central idea behind IODP Expedition
92 362. The main objective of the expedition was to collect core and log data of the incoming sedimentary succession
93 of the Indo-Australian oceanic plate to understand the seismogenic process related to the margin (Dugan et al.,
94 2017; McNeill et al., 2017). During the expedition in 2016, drilling was performed on two sites (U1480 and U1481)
95 located on the oceanic plate west of the North Sumatra subduction margin and east of the Ninety East Ridge
96 (Fig.1a, b) (Dugan et al., 2017). The drilling sites recovered a complete, 1.5 km thick sedimentary section from
97 late Cretaceous to Pleistocene down to the basement of basaltic crust (Dugan et al., 2017; McNeill et al., 2017).

98 The input sedimentary section of the Sumatra subduction zone comprises the distal part of the trench wedge,
99 Nicobar fan sequence, and pre-fan pelagic section on the basaltic crust at the bottom (Dugan et al., 2017; McNeill
100 et al., 2017). At Site U1480, the entire recovered section was categorized into six lithological entities, Units I to
101 VI (Fig. 1c) (McNeill et al., 2017). Unit I (0 to 26.72 mbsf) consists of unconsolidated calcareous clay, silty clay



102 with alternating fine sand (McNeill et al., 2017). Unit II from 26.72 to 1250 mbsf consists of alternating fine-
103 grained sand and silty clay to silt (McNeill et al., 2017). Unit III (1250 ~ 1327 mbsf) is divided into two subunits:
104 Unit IIIA and IIIB (McNeill et al., 2017). Unit IIIA consist of thin to medium-bedded, gray-green or brown
105 mudstone and intercalated siltstone, and Unit IIIB is composed of reddish-brown tuffaceous silty claystone with
106 fragmented sponge spicules and radiolaria (McNeill et al., 2017). The boundary between Units IIIA and IIIB (1310
107 mbsf) at this site marks the base of the Nicobar Fan and the beginning of the thin pre-fan succession (Pickering et
108 al., 2020). Units IV, V, and VI include volcanoclastic rocks with tuffaceous sandstone, conglomerates, and basaltic
109 oceanic crust, respectively. For this study, we restricted ourselves to the Nicobar fan sequence that comprises Unit
110 I, II, and IIIA. At Site U1481, the pre-fan succession was not encountered and a Unit III, a thicker equivalent of
111 Subunit IIIA at Site U1480, represents the material of the lower Nicobar Fan (see Figure F15, in Site U1481 report;
112 McNeil et al., 2017).

113 X-ray diffraction (XRD) and bulk rock analysis at Site U1480 (in Units I and II) show a clay mineral assemblage
114 dominated by illite, with minor smectite and chlorite (Supplementary data-1) (Rosenberger et al., 2020). The
115 smectite content decreases with depth with the mean value of 33 wt% in Unit I and 17 wt% in Unit II (Table 1)
116 (Rosenberger et al., 2020). However, the relative abundance of smectite content increases sharply in Unit IIIA
117 with a mean value of 73 wt%. The illite percentage in the clay assemblage increases down section from Unit I to
118 Unit II from a mean of 49 wt% to 59 wt%; whereas decreases in Unit IIIA with a mean of 19 wt%. The
119 expandability of the illite/smectite mixed-layer increases down-section, which signifies an opposite trend to the
120 one expected for burial diagenesis (Rosenberger et al., 2020). Clay mineralogy in the lower fan muds of Unit III
121 of Site U1481A contains an average of 37 percent smectite and 37 percent illite (Rosenberger et al., 2020).

122 The Nicobar fan sequence exhibits almost compositionally homogeneous (silt/clay ratio; mostly 'silty-clay')
123 subunits with uniform grain size (McNeill et al., 2017), and also a history of rapid deposition (125-290 m/my;
124 Backman et al., 2019). The drilling sites are 255 km away from the deformation front, thus the samples are
125 undisturbed by tectonic faulting. In addition, the scarcity of biogenic grains and low temperatures (<68°C) make
126 cementation only as highly localized concretions (McNeil et al., 2017; Torres and Milliken, 2019). Such a
127 homogeneous sedimentary secession extending across 1.5 km depth is rare in sedimentary basins. Hence, these
128 samples provide us with a unique opportunity to study depth-wise variation in microstructure as a function of
129 vertical effective stress with few complications from multiple causes of porosity loss.

130 Sampling and Methods

131 This study is based on two sample sets that were obtained from Sites 1480 (Holes E, F, G, and H) and 1481 (Hole
132 A) independently, and analyzed by slightly different methods. The first sample set (33 mud samples; depth 1.24
133 to 1300 mbsf) was prepared and analyzed using BIB-SEM at RWTH Aachen University, Germany. The second
134 sample set (22 samples; depths 6.25 to 1493.30 mbsf) was prepared using Ar-ion cross-section polishing and
135 imaged by field-emission SEM at the Bureau of Economic Geology (BEG) at the University of Texas at Austin.
136 Core description of the analysed 55 mud samples are tabulated in Supplementary data-2.



137 [BIB-SEM technique \(analysis of the first set of samples, Aachen University\)](#)

138 [Sample preparation for BIB-SEM and imaging](#)

139 We received 33 freeze-dried mud samples from the IODP repository, Japan (SN-1 to SN-33 in Table-1). The
140 samples were collected using a tube inserted perpendicular to the cut face of the drill core in such a way that the
141 notch of the tube identified the top of the sample so the orientation of bedding planes for each sample was known.
142 In Fig. 1d, a tube sample received from the IODP repository is shown, where the red line on the top of the tube
143 identifies the notch. Subsamples ($10 \times 5 \times 2 \text{ mm}^3$) were cut from the individual freeze-dried samples using a razor
144 blade. These subsamples were pre-polished using silicon carbide (SiC) paper to reduce the roughness of the surface
145 down to $10 \mu\text{m}$. Further, Broad Ion Beam (BIB) polishing was carried out using a JEOL SM-09010 cross-section
146 polisher for 10 hours at 6 kV and $150 \mu\text{A}$. BIB reduces surface damage by removing a $100 \mu\text{m}$ thick layer to
147 generate a high-quality polished cross-section of $1\text{-}2 \text{ mm}^2$ with a topography less than 5 nm (Desbois et al., 2009).

148 After polishing, the BIB cross-sections were coated with tungsten and imaged with a Zeiss Supra 55 SEM with
149 SE2, BSE, and EDX detector (Supplementary data-3). SE2 images were used to image porosity, while for
150 identifying phases BSE images are combined with an EDX map as well as EDX point analysis. For each cross-
151 section, we made mosaics of hundreds of SE2 and BSE images at a magnification of $20,000\times$ ($\sim 14.3 \text{ nm}$ pixel
152 value) and $10,000\times$ respectively, with an overlap of 20% to 30%, (Klaver et al., 2012; 2015; 2016; Hemes et al.,
153 2013; 2015; 2016; Laurich et al., 2014). The mosaics are stitched together using Aztec software preserving the
154 original pixel resolution. Finally, these stitched images are used for the segmentation of pore spaces, minerals, and
155 other respective analyses.

156 [Image segmentation and pore analysis](#)

157 For quantifying porosity and pore morphology, individual SE2 image mosaics were segmented using a ‘seed and
158 grow’ algorithm (Adams and Bischof (1994)) implemented with a MatLab code (Jiang et al., 2015; Schmatz et al.,
159 2016) (Supplementary data-3). The ‘seed and grow’ algorithm works based on the difference in intensity of
160 greyscale value in an image (Bright = minerals, dark = pores). After automatic segmentation, individual pores in
161 SE2 images are manually corrected if required.

162 Similarly, using ImageJ software (threshold toolbox and machine learning algorithm), segmentation of the
163 individual mineral phases was carried out combining BSE images and EDX elemental maps. While quartz, calcite,
164 pyrite, mica minerals are efficiently segmented using these tools, feldspars are found difficult to segment because
165 of similar composition as clay (Supplementary data-4, 5 and 6). Finally, corrected pore segmented SE2 mosaics
166 are overlaid on the phase maps using the ‘georeference’ tool of QGIS (<http://qgis.osgeo.org>), (Supplementary data-
167 4, 5 and 6).

168 [Pore detection resolution \(PPR\) and representative area analysis \(REA\)](#)

169 ‘Practical pore detection resolution’ (PPR) indicates the pore sizes above which one can assume to detect 100%
170 of the pores present in the SE2 mosaic (Klaver et al., 2012). In agreement with earlier results using this instrument
171 (Klaver et al., 2012; 2015; 2016; Hemes et al., 2013; 2015; 2016; Laurich et al., 2014), we found PPR of ~ 2000



172 nm² and ~8500 nm² for the magnification of 20,000x and 10,000x images, respectively, corresponding to 10pixel
173 ~~size in an image.~~

174 After segmenting all minerals, representative elementary area analysis (REA) was performed using the box
175 counting technique on mineralogical phase maps (Kameda et al., 2006; Klaver et al., 2012). Similar steps are also
176 followed for determining a representative elementary area for SE2 images. The estimated REA values using SE2
177 and BSE mosaics for the analysed 33 mudstone samples are documented in Supplementary data-7.

178 [Ion polishing and SEM technique \(second set of samples; BEG, UT Austin\).](#)

179 22 Samples (SN-34 to SN-55 in Table-1) were taken shipboard from the sample half of the still-wet core in small
180 plastic tubes (similar to the ones used for the sample set at Aachen) inserted into the core by manual pressure. The
181 tubes were removed from the core and sealed in plastic bags. In the laboratory at the BEG, sample bags were
182 opened and the muds were allowed to dry slowly in the tubes over several weeks. No discernible shrinkage was
183 observed as the dried core pieces still fully filled the tubes. The tubes were carefully removed and a small cube
184 (approximately 0.5 to 1 cm³) was cut using a sharp knife and small hand saws; an orientation mark was placed on
185 the cube to indicate the bedding direction. Bed-perpendicular surfaces were prepared by Ar-ion cross-section
186 polishing, using the Leica EM TIC020 triple ion beam miller and coated with Ir for imaging. Manual placement
187 of the cut cubes into the ion mill is not precise so the ion-polished surfaces have slight variation from perpendicular
188 to bedding. Pore imaging was performed on the FEI Nova NanoSEM 430 using the in-lens SE detector, a 30 μm
189 aperture, 15 KeV accelerating current, a working distance of around 5–6 mm, and an intermediate-range sample
190 current (spot size = 3, mid-range for the instrument). Randomly selected views (typically 3-6) of all samples were
191 collected at 6kx machine magnification; additional views illustrating pore types and pore/grain relationships were
192 made at 10kx to 30kx (machine magnification).

193 Results

194 [Estimating compaction strain from MAD-porosity data](#)

195 Shipboard MAD (moisture and density) porosity versus depth data for mud samples exhibits a sharp reduction in
196 porosity from 80% to 52% from the seafloor to 28 mbsf (Fig.2a). Deeper samples display a comparatively smaller
197 reduction in porosity of approximately from 52% to 30% over a depth range of 28 to 1500 mbsf (Fig.2a and b).

198 We calculated compaction strain using the shipboard MAD porosity data following a method proposed by [Nollet](#)
199 et al., 2005, and subsequently used by Neagu et al., 2010 (Fig.2c and d), assuming 1D consolidation and no change
200 in solid volume. The compaction strain (ϵ_c) is then computed as:

$$201 \quad \epsilon_c = \frac{1-\phi_0}{1-\phi_1} \quad (\text{Eqn-1})$$

202 Here ϕ_0 = initial porosity, and ϕ_1 = final porosity. Our samples from sites U1480 and U1481 show no evidence of
203 tectonic faults (McNeill et al., 2017), supporting our assumptions. We considered the initial porosity ϕ_0 as the
204 MAD porosity at 0.6 mbsf depth ($\phi_0 = 80\%$). Compaction strain following Eqn-1 (Supplementary data-7), is



205 plotted against depth in Fig. 2c and d. Compaction strain increases from 1 to 2.05 from the seafloor to 28 mbsf
206 (i.e. Unit I), and from 2.00 to 3.05 from 28mbsf to 1500 mbsf (Fig. 2c and d).

207 Another common measure of compaction is the intergranular volume (IGV; Paxton, 2002), which corresponds to
208 the sum of intergranular porosity and intergranular cement. In some mudstones, it may be necessary to calculate
209 IGV differently because of the presence of abundant primary intragranular pores and pore-filling bitumen
210 (Milliken and Olson, 2017). In our sample set, cement is absent, and IGV is taken to equal the bulk porosity from
211 shipboard MAD measurements.

212 Compactional porosity loss (COPL), referenced against the original sediment volume, is calculated from the initial
213 primary intergranular porosity (P_i ; 80% in this case) and the IGV as follows (Lundegard, 1992; Ehrenberg, 1989):

$$214 \text{COPL} = P_i - \left(\frac{(100 - P_i) \times \text{IGV}}{100 - \text{IGV}} \right) \quad (\text{Eqn-2})$$

215 At an IGV of 50%, COPL is 60%; in the deepest samples in the Nicobar fan (IGV of around 30%) COPL is 70%
216 (supplementary data-7). ~~Contribution of cementation (CEPL) is absent in the absence of observed cements.~~

217 Description of grain microstructure and pore morphology

218 To have consistency in the data set, we prepared SE2 mosaics for all samples from the Aachen sample set at
219 20,000x magnification covering an average $100 \times 100 \mu\text{m}^2$ area (Supplementary data-7). In addition, to examine
220 the effect of magnification on BIB-SEM porosity and representative area analysis (REA), three samples (i.e. SN-
221 7, SN-15, and SN-29) were also imaged each at 5,000x and 10,000x magnification (Supplementary data-7),
222 respectively. A decrease in magnification and resolution reduces visible BIB-SEM porosity.

223 We observed consistent results for the REA analysis. For SE2 mosaics REA varies between $45 \times 45 \mu\text{m}^2$ to 85×85
224 μm^2 at 20,000x magnification, and for segmented phase maps, REA varies between $90 \times 90 \mu\text{m}^2$ to $130 \times 130 \mu\text{m}^2$
225 at 10,000x magnification (Supplementary data-7). In the UT sample set, the standard images taken at 6kx with
226 machine magnification are $49.7 \times 45.7 \mu\text{m}^2$, so these images are also within the estimated REA range.

227 Six mineral phases occur in significant amounts in the Sumatra samples, as detrital particles: quartz, feldspar (K-
228 feldspar, albite, and Ca-plagioclase), calcite, micas (muscovite, biotite, and chlorite), and detrital ~~clay~~-clay-size
229 particles, which are dominantly illite. The average clay percentage in these mudstone samples varies between 65%
230 to 75%. Samples SN-1 (77%) and SN-4 (76%) are slightly enriched in clay content, whereas SN-7, SN-9, SN-17,
231 SN-28, SN-29, and SN-31 contain less clay (<65%) (Supplementary data-7).

232 Using BIB-SEM and automatic pore segmentation techniques, an average of >30,000 pores ~~have~~ been detected
233 for each individual sample in the Aachen sample set at 20,000x magnification. Correlating with the MAD data set,
234 the estimated BIB-SEM porosity reduces from 32% to 19% over a depth range of seafloor to 28 mbsf, while the
235 deeper samples display a smaller reduction from 19% to 10% over a depth range of 28 to 1500 mbsf respectively
236 (Fig.3a). Consistent with numerous previous studies, the results document a mismatch between bulk measured
237 porosity (MAD) and imaging porosity (BIB-SEM) (e.g., Hemes et al., 2013; Houben et al., 2014; ~~Nole~~ et al., 2016;



238 Olkar et al., 2019) (Supplementary data-7). We plotted BIB-SEM porosity vs MAD porosity and found an
239 approximately linear correlation (Fig. 3b).

240 Type of pores

241 Intergranular pores contribute >99% of the total visible porosity (Fig.4). Intragranular pores (see below) are rare.
242 The size and shape of inter-granular pores change during compaction (Table 2).

243 Intergranular pores are classified based on grain size (irrespective of mineralogy): 1) Clay domain (matrix) pores,
244 and 2) Silt-adjacent pores. Based on the variation in size, clay domain pores divided further into: 1) Large clay
245 domain pores; pore size $>5 \times 10^5 \text{ nm}^2$, and the pore boundary is defined by more than three clay particles, and 2)
246 small clay domain pores; the pore size $<5 \times 10^5 \text{ nm}^2$ and generally occur in between two/three clay particles (see
247 further detail below). Large and small clay domain pores are classified by geometry as: 1) Elongate pores (aspect
248 ratio $>3:1$) and, 2) equant-shaped pores (aspect ratio $<3:1$). Elongate pores consist of: 1) linear-elongated pores,
249 and 2) crescent-shaped elongated pores. Examples of different clay-domain pore types are shown in Fig. 5, 6, and
250 7.

251 Silt-adjacent are categorized as two types: 1) large silt-adjacent pores are $>5 \times 10^5 \text{ nm}^2$, and pore boundaries are
252 defined by more than three particles; and 2) small silt-adjacent pores include pore sizes $<5 \times 10^5 \text{ nm}^2$, and pore
253 boundaries are defined by two/three particles (see further detail on the modal sizes of these pore types below).
254 Large and small silt-adjacent pores are either: 1) Equant shaped (aspect ratio $<3:1$) or 2) elongated (aspect ratio
255 $>3:1$). Further, elongated silt-adjacent pores consist of: 1) linear-shaped elongated pores and 2) crescent-shaped
256 elongated pores. These pore types are highlighted in Fig. 5, 6, and 7.

257 Change in inter-particle pore morphology with depth

258 Seafloor to 28mbsf (Unit I)

259 The shallow mud samples in Unit I are unconsolidated and highly porous (Fig. 5a; Supplementary data 8). Sample
260 SN-1 (1.24 mbsf) has a maximum MAD porosity of 80%. We observe three types of clay particle contacts in the
261 microstructure of SN-1; edge to edge (EE), edge to face (EF), and face to face (FF) contacts. Among them, EF and
262 FF contacts are abundant and EE contacts are rare (Table 2). The sample exhibits abundant large clay domain
263 pores and large silt-adjacent pores that are equant with smooth edges and a rounded pore perimeter. The sample
264 also contains abundant linear-elongated and equant-shaped small clay-domain pores. Crescent-shaped small clay
265 domain pores are rare in the microstructure of this sample. Equant-shaped, small silt-adjacent pores are abundant.
266 In addition, linear elongated and crescent-shaped small, silt-adjacent pores are also commonly observed (Fig.5a;
267 Table 2).

268 With increasing compaction strain ($\epsilon_c = 1.119$) and depth (5.1 mbsf; Supplementary data 8), porosity (MAD)
269 reduces to 75% and corresponding COPL=19% (sample SN-2; Fig. 5b). The microstructure of SN-2 displays
270 almost similar characteristics as observed in the earlier sample SN-1, although there are fewer large clay domain
271 pores in SN-2 than SN-1. Linear elongated and equant-shaped small clay domain pores are common (Table 2), but



272 crescent-shaped small clay domain pores are rare. The microstructure of SN-2 exhibits abundant equant-shaped
273 large and small silt-adjacent pores.

274 With an increase in compaction strain to $\epsilon_c \sim 2.00$ (28 mbsf), the sample microstructure is dominated by FF contacts
275 (Fig. 5c), and EE and EF contacts are rare (Table 3). Additionally, large clay-domain pores become sparse or
276 infrequent in the microstructure (Fig. 8). Crescent-shaped, small clay domain pores in the microstructure are rare,
277 whereas equant-shaped small clay domain pores are common. Both small and large silt-adjacent pores exhibit
278 equant shapes (Fig. 8d, e and f). The sample analysed at the base of Unit I (SN-6; 28 mbsf) contains rare large
279 clay-domain pores and abundant FF contacts (Fig. 5c; MAD porosity = 54% and COPL = 55%).

280 *28 mbsf to 1500 mbsf (Units II and III)*

281 Mud samples from the lower part of the Nicobar fan section are more compacted than shallower samples. We
282 analyzed a total of 29 samples using BIB-SEM at Aachen and 18 samples using the field emission SEM at UT
283 Austin from this section. An increase in compactional strain from 2.00 to 3.15 over a depth range of 28 to 1500
284 mbsf causes a porosity reduction (MAD) of 54% to 28%, and the corresponding change in average COPL is 55%
285 to 72%. The microstructure of these samples is dominated by FF contacts among clay particles; EF and EE contacts
286 are rare (Table 3; Fig. 6 and 7 b, c). All samples exhibit abundant small linear-elongated clay domain pores between
287 two parallel clay sheets (Fig. 8b). Equant-shaped small, clay domain pores are rarely observed below 150 mbsf
288 depth ($\epsilon_c > 2.4$). Crescent-shaped, small, clay domain pores are rare at shallow depth but become abundant with an
289 increase in compactional strain $\epsilon_c > 2.95$ (871.87 mbsf) as the surrounding clay particles are bent (Fig.6;
290 Supplementary data 9). In addition, large clay domain pores in these samples are rarely observed in the vicinity of
291 silt clasts (Table 2).

292 Below 100 mbsf ($\epsilon_c = 2.20$), silt-adjacent small pores are dominantly equant shaped, but below 300 mbsf ($\epsilon_c > 2.5$)
293 silt-adjacent small pores are dominantly linear-elongated (Fig. 8e). Crescent-shaped, small, silt-adjacent pores are
294 common in all samples. Large silt-adjacent pores are dominantly equant above 200 mbsf depth ($\epsilon_c < 2.40$) and
295 commonly linear-elongate below 400 mbsf depth ($\epsilon_c > 2.5$) (Fig.8f). It appears that due to an increase in
296 compactional strain the shape of the silt-adjacent pores changes from equant to linear-elongated (Table 2). In
297 samples with more silt, equant-shaped small and large, silt-adjacent pores can persist at greater depths (Fig. 8e and
298 f).

299 Below 28 mbsf ($\epsilon_c > 2.0$), the number of large silt-adjacent pores in the microstructure decreases. Comparing
300 samples SN-8 (74.07 mbsf and $\epsilon_c = 2.09$) and SN-32 (1267.14mbsf and $\epsilon_c = 3.15$) illustrates how the number of
301 large, silt-adjacent pores decreases with depth (Fig. 6a, and c) when the clay fraction (Supplementary Data 7) is
302 comparable. This relationship is apparent even in samples separated by a smaller depth difference (SN-49 from
303 959.14 mbsf and SN-55 from 1433.36 mbsf; Fig. 7b and c). While the number of large pores diminishes, the
304 maximum size of the large silt-adjacent pores remains constant (10^7 nm^2 ; Supplementary data 10).



305 Intra-particle and intra-crystalline pores

306 Intraparticle pores are observed in microfossils, authigenic pyrite framboids, equant-shaped dolomite, calcite,
307 quartz, mica, and lithic grains. Two different types of intraparticle pores were found in microfossils; elongated
308 pores (Supplementary data 11a and c) and large rounded pores (Supplementary data 11b and d). The typical size
309 of the elongated and rounded pores in microfossils (10^5 nm^2) are larger than elongated pores (10^3 nm^2). While
310 intraparticle pores in microfossils and most detrital grains are present at deposition, intraparticle pores in many
311 mica grains form during burial and are considered secondary pores. Intraparticle pores in micas have cleavage-
312 parallel, elongated pores with an aspect ratio >7 (Supplementary data 11e), and are interpreted to open by bending
313 of the micas during compaction (Supplementary data 11f).

314 Variation in the orientation of pores and grains due to compactional strain

315 We examined the change in orientation of the long axis of pores with increasing compaction strain. For all
316 segmented pores, the angle between the long axis and the bedding plane was determined and plotted in rose
317 diagrams (Supplementary data-12). Samples from the seafloor to 28 mbsf exhibit a weak preferred orientation of
318 the long axis of pores with maxima oriented obliquely to the bedding planes. However, below 28 mbsf the samples
319 have a preferred orientation of the long axis of pores aligned subparallel to the bedding plane. Further, due to an
320 increase in vertical effective stress down section below 28 mbsf in Units II and III, the degree of preferred
321 alignment of the long axis of pores only increases a small amount (Supplementary data-12).

322 We determined the angle between the long axis of individual silt grains and the bedding plane for all samples and
323 plotted the angle in a rose diagram (Supplementary data-12). For quartz, feldspar, and calcite the degree of
324 preferred orientation of the long axis of grains changes little with depth. However, the rose diagrams obtained for
325 mica show a weak maxima parallel to the bedding plane and several submaxima oriented obliquely to the bedding
326 plane above 28 mbsf. Preferred alignment of the long axis of mica grains increases at 28 mbsf with a strong
327 maximum oriented parallel to bedding plane. Below 28 mbsf, further increase in the degree of preferred alignment
328 is small.

329 Size distribution of pores

330 Pore size distributions (Fig.9) of shallow samples (Unit I) are trimodal. Sample SN-1 has peaks between 10^5 to
331 10^6 nm^2 , 10^6 to 10^7 nm^2 , and 10^7 to 10^8 nm^2 , and SN-2 has peaks from 10^4 to 10^5 nm^2 , 10^5 to 10^6 nm^2 , and 10^6 to
332 10^7 nm^2 . These three pore size regimes correspond to the small clay domain and silt-adjacent pores, large clay
333 domain pores, and large silt-adjacent pores. Samples from Units II and III exhibit bimodal pore size distributions
334 (SN-10, SN-26, and SN-33 in Fig.9). SN-10 has a peak between 10^5 to 10^6 nm^2 , corresponding to small clay
335 domain and silt-adjacent pores, and 10^6 to 10^7 nm^2 , reflecting large silt-adjacent pores. Large clay domain pores
336 are absent from samples below 28mbsf depth (Units II and III) based on the pore size distributions combined with
337 image analysis. At the shallow depth, contribution to total porosity by larger silt-adjacent pore is greater compared
338 to the contribution by small clay domain pores (Fig.9 e and g). The contribution of large, silt-adjacent pores to
339 total porosity diminishes with depth. Hence, at greater depth, contribution to total porosity by larger silt adjacent
340 pore is less compared to small clay domain pores (Fig.9i).



341 Pore size distributions follow a power-law shown on a double logarithmic graph following the equations (Klaver
342 et al., 2012; 2015; 2016; Hemes et al., 2013; 2015; 2016; Laurich et al., 2014):

$$343 \frac{N_i}{b_i S_{mosaic}} = C S_{pore}^D \quad (\text{Eqn-3})$$

$$344 \log\left(\frac{N_i}{b_i S_{mosaic}}\right) = -D \cdot \log(S_{pore}) + \text{Log } C \quad (\text{Eqn-4})$$

345 Where N_i = number of pores with area S_{pore} , b_i = bin size, S_{mosaic} = surface area of the current mosaic,
346 C =constant, and D = power-law exponent. The resulting power-law exponent (D) varies between 1.70 to 2.00
347 (Supplementary data-7).

348 [Effect of texture on porosity, pore morphology, and orientation of pores](#)

349 We analyzed six samples (SN-7, SN-9, SN-17, SN-28, SN-29 and SN-31) that are enriched in silt content compared
350 to the rest of the mud samples (Supplementary data-7). Silt content has a positive correlation to the total SEM
351 porosity. For example, sample SN-29 (1172.88 mbsf) exhibits a BIB-SEM porosity of 14% whereas other samples
352 from a similar depth with less silt exhibit an average BIB-SEM porosity of 12% (Supplementary data-7) at 20000x
353 magnification. The samples with greater silt content are also enriched in equant-shaped silt-adjacent larger pores
354 (Supplementary data 13a). We also estimated the orientation of the long axis of pores for these three samples and
355 plotted the obtained results as rose diagrams (Supplementary data 13b). The obtained results exhibit a relatively
356 weak preferred alignment of the long axis of pores with respect to the bedding planes (Supplementary data 11b).

357 [Discussions](#)

358 [Effective stress vs porosity: A comparison with experimental study](#)

359 To understand the consolidation mechanisms of the Sumatra sediment we estimated vertical effective stress
360 following the steps proposed by Hüpers et al., 2015. Following Tarzaghi and Peck (1948) vertical effective stress
361 is expressed as:

$$362 \sigma_v' = \sigma_v - P_f \quad (\text{Eqn-7})$$

363 Here σ_v = total vertical stress caused by the overburden load, and P_f = fluid pressure. To compute vertical effective
364 stress of a layered sediment, we use Eqn 8:

$$365 \sigma_v' = \sum(\rho_s - \rho_w) \cdot g \cdot \Delta z \quad (\text{Eqn-8})$$

366 where ρ_s = bulk density of the sediment, ρ_w = density of the pore water, Δz = depth interval, and g = gravitational
367 acceleration. During IODP Expedition 362, drilling was performed 255 km away from the deformation front.
368 Although small offset strike-slip faults are evident at the seafloor and in seismic reflection profiles (McNeill et al.,
369 2017), the amount of strain attributed to these fault offsets is compatible with the idea that the maximum
370 horizontal stress is comparable to the vertical stress; there is no evidence in seismic reflection data or from core



371 microstructures for thrust or reverse faults associated with a vertical least principal stress. On this basis, we assume
372 that vertical effective stress is the maximum principal stress. Bulk density of the sediment ρ_s was obtained from
373 McNeill et al., (2017), and ρ_w was considered as the density of sea-water i.e. 1025 kg/m³ (Hüpers et al., 2015).

374 We plotted vertical effective stress vs MAD porosity of 55 mud samples (Fig. 10). Fawad et al. (2010)
375 experimentally studied the consolidation behavior of mud with varied proportions of silt and clay. While Sumatra
376 samples follow trends similar to those defined by Fawad et al. (2010), the experimental samples are more
377 compacted than natural Sumatra samples for the same silt content.

378 Clay mineralogy has a significant effect on the compaction behavior of mudstone (Mondol et al., 2007). Mondol
379 et al. (2007) performed compaction experiments using pure smectite and pure kaolinite clay particle packs; as they
380 represent two end members compared to other clay minerals (illite and chlorite) in terms of grain size and surface
381 area. Smectite is the most fine-grained clay and has the largest surface area; whereas kaolinite is the coarsest one
382 and has smaller surface area among all other clay mineral types (Meade, 1963; Mesri and Olson, 1971; Rieke and
383 Chilingarian, 1974). Hence, kaolinite is more compressible than smectite, and clay compaction gradually decreases
384 with increasing the proportion of small size clay particles in the sample (Mondol et al, 2007).

385 Fawad et al., (2010) used clay mixtures of 81% kaolinite, 14% mica, and 5% microcline grains, whereas Sumatra
386 mud samples are mainly composed of >73% of illite and lesser smectite, with only <16% undifferentiated chlorite
387 and kaolinite, and <7% quartz particles. Therefore, due to higher illite/smectite content, Sumatra muds appeared
388 to be less compacted compared to the experimental samples used by Fawad et al. (2010).

389 BIB-SEM porosity vs MAD porosity

390 We note that BIB-SEM porosity is lower than the porosity found from the shipboard MAD data, however the two
391 measurements correlate along a line through the origin. (Fig.3b). The reason for this difference is that MAD
392 porosity measures the total amount of moisture in a much larger sample and accounts for pores much below the
393 PPR and also rare large pores not included in the 1 mm² BIB section. Earlier studies also documented and discussed
394 mismatch between MAD and BIB-SEM measurements (Hemes et al., 2013; Houben et al., 2014; Nole et al., 2016;
395 Olkar et al., 2019). We plotted estimated BIB-SEM porosity and MAD porosity data from earlier studies on BOOM
396 clay (Hemes et al., 2013; Olkar et al., 2019); Opalinus clay (Houben et al., 2014); and samples from Nankai trough
397 (Nole et al., 2016). The data for Boom clay and Opalinus clay follow similar trend as Sumatra samples, whereas
398 clay samples from Nankai trough shows different trend, and it could be attributed due to the difference in
399 magnification of imaging of Nankai samples.

400 In addition we plotted clay content vs the difference between the two porosities in Supplementary data 14a. We
401 performed regression analysis using the data set for the 33 muds samples analyzed at Aachen (Supplementary data
402 14b). First, only two variables i.e., BIB-SEM porosity vs MAD porosity (following Eqn-5); second, we considered
403 three variables MAD porosity, BIB-SEM porosity, and clay content (following the Eqn-6).

404 BIB-SEM porosity = a * MAD porosity + c (Eqn-5)



405 $\text{BIB-SEM porosity} = a * \text{MAD porosity} + b * \text{clay content} + c$ (Eqn-6)

406 The coefficient of determinations (R^2) for Eqn-5 and Eqn-6 are 0.8408 and 0.9262 respectively. These results
407 show that the ratio in porosity depends on depth and clay content.

408 For all samples the BIB-SEM pore size distribution follows power-law over an interval of three orders of
409 magnitude. We may extrapolate this below the practical pore resolution (PPR). (Klaver et al., 2012; Kuila and
410 Prasad, 2013; Wang et al., 2019). Extrapolating our data set down to 3nm pore diameter, it is found that BIB-SEM
411 porosity increases only up to 20%~25%. So, there is still an average mismatch of 15% to 20% between the MAD
412 porosity and extrapolated BIB-SEM porosity. The fall off from the normal trend in log-log pore size distribution
413 plots (Fig.9b) for the shallow depth (Unit-I) samples suggest that also large pores are uncounted in the data set.
414 The mud samples from Unit-I contains forams that are rare or absent in the deeper section (Supplementary data-
415 11a, b, c, and d), and missing pore volume can be attributed to the intact forams that may be missed due to the
416 small size of the BIB SEM sample. Moreover, shallow depth samples are richer in smectite compared to the deeper
417 samples, which can also somewhat ~~influence to overestimate~~ the MAD porosity.

418 [Micromechanical model for porosity reduction](#)

419 [Sharp reduction in porosity at the shallow depth from the seafloor to 28 mbsf](#)

420 High porosity (80% MAD; 32% BIB-SEM) in the shallowest sediments is attributed to large pores in the samples
421 created by abundant EE and EF particle contacts (Fig. 5a and 7a). These contacts are unstable and collapse to form
422 FF contacts, resulting in a rapid porosity decrease ~~with 28m of burial~~ (Table 3). This deformation is apparent from
423 the reduction in large clay domain pores observed over this interval (Fig. 8; Table 2). Collapse of pores surrounded
424 by EE and EF contacts is further recognized by the progressive alignment of clay particles into the bedding plane
425 and by the **increase number and consistent orientation** of elongated, small, clay domain pores. Each of these
426 observations is consistent with rotation of clay particles into the bedding plane as these large clay domain pores
427 collapse.

428 [Mechanism of porosity reduction from 28 mbsf to 1500 mbsf](#)

429 Below 28 mbsf to >1500 mbsf, porosity continues to decrease from 50-32% (MAD) but at a reduced pace. SEM
430 observations suggest that this porosity decline results from the progressive loss of silt-adjacent pores with large
431 silt-adjacent pores lost before small ones (Fig. 8), although they remain present in common abundance to 1200
432 mbsf. Small, clay domain pores are abundant throughout the section, and the large clay domain pores were lost
433 above 28 mbsf.

434 Within the population of silt-adjacent pores, the large, equant pores are most susceptible to collapse (Fig. 8). Large,
435 elongate pores persist in abundance, both in linear and crescent geometries. While it seems plausible that large,
436 equant pores collapse to form large, elongate pores, no corresponding increase in the elongate pore population is
437 observed. Large, elongate pores may collapse further and become small silt-adjacent pores. Microstructural
438 evidence supports the idea that large equant pores collapse as surrounding clay aggregates bend and shrink the size
439 of the remaining pore (Fig. 11a to f), and that the collapse results in an increasing aspect ratio of the pore. While



440 initial pore shrinkage may be accommodated solely by the bending of clay particles above the pore (Fig. 11),
441 further collapse may require clay particles to slide into the pore (Fig.11g-iii) or become fractured (Fig.11g-v) in
442 order to allow clay to invade the pore (model shown in Fig.11 is elaborately described in Supplementary data-15).

443 Small, silt-adjacent pores also become less abundant with burial, but the transition occurs deeper than the large
444 pores, and small, silt-adjacent pores remain common throughout the section (Fig. 11). **Equant, small pores are lost**
445 **like the large pores, and elongate pores remain abundant within this population subset throughout.** There is a loose
446 correspondence between the loss of small, equant pores and an increase in elongate pores, suggesting that pore
447 flattening is part of the pore collapse history. The pore collapse evolution outlined for large pores (Fig. 11) appears
448 **to hold** for small pores, even though observations are more challenging.

449 Small, clay domain pores appear to remain resilient throughout the compaction history (Fig. 8), even though some
450 of these pores must become lost to account for porosity loss. Small, equant pores are lost between 100-200 m, and
451 this loss appears to be accommodated by an increase in elongate pores (Fig. 8). Elongate crescent pores increase
452 in abundance around 800 mbsf, and we interpret this to reflect folding of abundant linear elongate pores as the
453 overall system compacts.

454 Large, equant pores in the clay domain are lost within the first few 10's of meters of burial. Elongate pores appear
455 to form at the expense of equant pores, and there may be a reduction in pore size associated with this shape change.
456 Most of the pores remaining after 1500 m of burial are small, elongate pores found both in clay domain and silt-
457 adjacent pores.

458 The presence of silt particles locally redistributes the force chain of load to retain silt-adjacent, large pores
459 undeformed (Schneider et al., 2011). The samples with greater silt content are also enriched in equant-shaped silt-
460 adjacent larger pores (Supplementary data 13a) in the microstructure. Hence, and as a result, they display greater
461 porosity compared to other samples from similar depths intervals (Supplementary data-7).

462 Previous laboratory studies have emphasized the importance of clay particle rotation as a dominant mechanism for
463 mechanical compaction in mudstone (Bennett et al., 1981; Vasseur et al., 1995; Aplin et al., 2006; Day-Stirrat et
464 al., 2008; 2011). While we infer rotation is an important mechanism for mechanical compaction at the shallowest
465 depth where unstable EE and EF particle contacts are present, clay particle bending and sliding/fracturing are
466 considered more important for most of the section studied.

467 [Mechanical compaction of marine sediment: a conceptual model](#)

468 According to Emmanuel and Day-Stirrat (2020), the reduction of pores in sedimentary rocks during compaction
469 is size-dependent, larger pores deform much readily than smaller pores. According to their model, larger pores
470 rapidly decrease in size during compaction to reduce the overall porosity of the sample. However, microstructural
471 analysis of Sumatra samples suggests that porosity reduction is accomplished by compaction of all pore sizes.
472 **While large, clay domain pores are lost more quickly than large, silt-adjacent pores, silt-adjacent pores are larger**
473 **than clay domain pores.** Moreover, the maximum size of pores remains almost constant irrespective of increasing
474 vertical effective stress/depth (Supplementary data 8) with little difference observed for the maximum pore size in



475 samples from 98.25 mbsf and 1299.31 mbsf. The preservation of a constant ratio between MAD and BIB-SEM
476 porosity measurements (Fig. 3b) suggests that porosity loss is distributed across all pore sizes. We infer that all
477 pore sizes are available for compaction for every increment of applied stress but acknowledge that the rate of pore
478 reduction in different size classes may proceed at different rates.

479 We propose a new model for the reduction in porosity in which, all pores within the force chain of load take part
480 in the reduction in porosity during compaction irrespective of their size. At shallow depth up to 28mbsf, larger
481 clay-domain pores are the most susceptible to early response during an increase in compactional strain, because
482 of two reasons, 1) the ‘domains’ defined by the clay aggregate are weaker compared to the larger rigid silt grains,
483 and 2) due to higher relative proportion of clay-rich regions within the mud, the force chain of load dominantly
484 passes through the clay aggregate. The dispersed nature of the silt-size particles and the high proportion of
485 phyllosilicates in the mud samples indicate that soft clay particles act as the principal load-bearing framework.
486 Hence, larger clay domain pores are more unstable compared to silt adjacent pores in the mud microstructure.
487 Similarly, below 28mbsf ~~depth in Units II and III,~~ under an increase in vertical effective stress, both the larger silt-
488 adjacent pores and smaller pores in the clay matrix that come within the force chain of load collapse. Hence, the
489 ratio between BIB-SEM porosity vs MAD porosity remains almost constant irrespective of the depth. All larger
490 silt-adjacent pores do not come within the force chain of load at the same time. Hence, some of the larger silt-
491 adjacent pores remained undeformed to the maximum depth of 1500mbsf depth. Therefore, the maximum size of
492 the larger silt adjacent larger pores remains almost constant irrespective of the depth/vertical effective stress.

493 While our understanding of how different pore types is consistent with all available data, tracking the pore
494 evolution through additional size categories would elucidate the pore evolution in more detail. Preliminary pore
495 size distribution data (Fig.9) indicate that 4 size bins exist in these samples. Developing this approach requires
496 improved image analysis techniques to tie all the pore attributes together on a pore-by-pore basis for a huge number
497 of pores.

498 [Compaction strain accommodation and grain-scale deformation](#)

499 Deformation of clay-rich sedimentary rocks involves four possible mechanisms: 1) Particulate flow; (Morgenstern
500 and Tchalenko, 1967; Borradaile et al., 1981); 2) Cataclasis; (Ukar and Cloos, 2019) 3) Diffusive mass transfer;
501 (Blenkinsop, 2000; Fossen, 2016); 4) Intercrystalline plasticity (Blenkinsop, 2000; Fossen, 2016). The intensity
502 and occurrence of a particular deformation mechanism in mudstone depend on several parameters, such as
503 effective stress, water content, cementation, temperature (Desbois et al., 2017; Den Hartog and Spiers, 2014).

504 All our samples show evidence of particulate flow controlled by friction between grains. At shallow depths, illite
505 platelets contacted at EE and EF junctions lose these weak bonds, and particles rotate into bedding-parallel
506 orientation. Once FF contacts dominate, large-scale rotations are reduced and intra-crystalline slip becomes
507 important. This is best evidenced in collapse of large, silt-adjacent pores where bent clay particles overlie pores
508 (Fig.11). In deforming granular foam material, bending was reported as the dominant deformation mechanism for
509 the reduction in porosity and developing preferred alignment of the long axis of pores perpendicular to the applied
510 stress (Elliott et al., 2002, Zhou et al., 2004; Samsudin et al., 2017; Zakaria et al., 2018) (review of these earlier



511 studies on the experimental deformation of granular foam is described in supplementary data-16). Friction adheres
512 clay particles to the edge of pores while the middle of particles drops into the pore, resulting in bending by intra-
513 crystalline slip. A cartoon (Fig. 12g) illustrates the compaction mechanism associated with the bending of clay
514 particles. With increasing compaction strain, clay particles undergo bending, and as a result, pore area reduces and
515 the orientation of the pores tends to align perpendicular to the applied effective stress (Fig. 12g).

516 [Compaction of Sumatra input section: generalized implication for rock property](#) 517 [evolution](#)

518 The overall compaction curve obtained for Sumatra muds is comparable with the experimental study by Fawad et
519 al., 2010 in the context of compactional range (Fig.8). The curve shows a monoexponential decrease in porosity
520 with an increase in vertical effective stress, which is evidence of normal consolidation (Fawad et al., 2010;
521 Dutilleul et al., 2020).

522 The larger silt-adjacent pores seen in the deepest of these samples (1500 m burial) suggest these muds retain
523 considerable potential for additional compaction in deeper burial. As this marine sediment progressively
524 approaches greater burial at closer proximity of the accretionary prism, it will undergo further change in physical
525 and deformational properties (Bray and Karig, 1985). Despite the substantial compactional strain, the relatively
526 high porosity of the deepest sample and the survival of larger and mechanically unstable silt-margin pores suggests
527 that compactional stabilization has not been reached because such IGVs and pore types are not generally observed
528 in older and lithified mudrocks. Based on the current understanding of subduction zone deformation behavior and
529 mudrock properties, it seems likely that compaction will continue to dominate the pore loss in deeper burial.

530 The general absence of early cementation and the corresponding dominance of compaction in the total pore loss,
531 is consistent with observations of other siliciclastic-dominated muds (Milliken, 2014; 2019). The trends for
532 intergranular volume observed [across](#) the seafloor to 1500mbsf place useful constraints on the maximum cement
533 volumes that theoretically could be emplaced at this depth range in sediments containing a more reactive grain
534 assemblage. At the depths of burial attained at the deformation front, any cementation of the Sumatra input
535 sediments will be limited to <30% of the rock volume, or possibly much less, as compaction is expected to continue
536 up to the burial temperatures that initiate grain reactions and associated cementation.

537 [Conclusions](#)

538 Pores can be classified by size and also microstructural position. Their contribution to the total porosity is
539 multimodal.

540 Samples at shallow depth (seafloor to 28 mbsf) display a sharp reduction in porosity from 80% to 52% due to the
541 collapse of the large clay domain/matrix pores. Deeper samples (28 mbsf to 1500 mbsf) exhibit a smaller reduction
542 in porosity from 50% to 32% due to collapse of silt-adjacent pores by bending and subsequently fracturing/sliding
543 of clay aggregate.



544 Large equant pores in clay (between 10^6 and 10^7 nm²) are rare below the first few meters of burial, after the
545 flocculated structure collapses.

546 The class of large pores next to silt-size grains (between 10^4 and 10^6 nm²) remains common to >1 km burial,
547 irrespective of the mineralogy of the silt-sized grains, but their size decreases with depth. Small, equant pores next
548 to silt particles are abundant in the first 100 m of burial and remain common over the whole samples depth range.

549 Small pores in clay domains are almost all elongated, and abundant over all observed depths. Small, crescent-
550 shaped elongate pores increase in abundance with depth as clay particles become folded by compactional
551 processes.

552 The size-independence of pore loss arises because the force chain driving pore collapse is localized primarily
553 within the volumetrically dominant and weaker clay-rich domains; larger pores around isolated silt particles enter
554 into the force chain somewhat randomly and asynchronously and do not contribute preferentially to pore loss over
555 the depth range studied.

556 An increase in effective stress up to 18MPa (~1500 mbsf) causes the development of weakly aligned phyllosilicate
557 fabric (defined by mica and illite clay particles) in the microstructure.

558 Compaction processes in our samples are dominated by granular flow (rotation and frictional sliding of illite clay
559 particles) at shallow depths. With increasing depth, compaction is additionally accommodated by bending of clay
560 particles.

561 Data availability

562 High resolution SE2 and BSE images of all samples are available online at:
563 <https://figshare.com/s/cbaada517b0b1409d575>

564 Authors contributions

565 SL and KLM performed sample preparation and BIB-SEM microscopy. SL analysed the data. JLU and GD
566 acquired funding. JLU managed the project. PV, KLM and JLU significantly contributed to interpret the data. SL
567 wrote the first draft of the manuscript. PV, KLM and JLU contributed for the correction and improvement of the
568 manuscript.

569 Competing interests

570 The authors declare that they do not have any conflict of interest.



571 Acknowledgments

572 SL and JLU thank German Research Foundation (Deutsche Forschungsgemeinschaft [DFG] grant UR 64/19-1)
573 for providing funding to carry out the research. IODP (International Ocean Discovery Programme) sample
574 repository, Japan is acknowledged for providing oriented mud samples for the study. KLM acknowledges the
575 samples and data provided by the International Ocean Discovery Program (IODP). Funding for sample preparation
576 and SEM imaging was supported by a post-expedition award (Milliken, P.I.) from the Consortium for Ocean
577 Leadership. SL thanks Manuel Menzel, Jop Klaver, Liene Spruženiece, and Joyce Schmatz for providing valuable
578 time to teach BIB-SEM techniques.

579 References

- 580 Ajdukiewicz, J. M. and R. H. Lander 2010. Sandstone reservoir quality prediction: state of the art. AAPG Bulletin
581 94: 1082-1091.
- 582 ~~Alam, M., Alam, M.M., Curray, J.R., Chowdhury, M.L.R. and Gani, M.R., 2003. An overview of the sedimentary
583 geology of the Bengal Basin in relation to the regional tectonic framework and basin-fill history. Sedimentary
584 geology, 155(3-4), pp.179-208.~~
- 585 ~~Al-Mukhtar, M., Belanteur, N., Tessier, D., and Vanapalli, S.K. (1996). The fabric of a clay soil under controlled
586 mechanical and hydraulic stress states. Appl. Clay Sci. 11, 99–115.~~
- 587 Ammon, C.J., Ji, C., Thio, H.K., Robinson, D., Ni, S., Hjorleifsdottir, V., Kanamori, H., Lay, T., Das, S.,
588 Helmberger, D. and Ichinose, G., 2005. Rupture process of the 2004 Sumatra-Andaman
589 earthquake. science, 308(5725), pp.1133-1139.
- 590 Aplin, A. C., I. F. Matenaar, D. K. McCarty and B. A. van der Pluijm 2006. Influence of mechanical compaction
591 and clay mineral diagenesis on the microfabric and pore-scale properties of deep-water Gulf of Mexico mudstones.
592 Clays and Clay Minerals 54: 514-500.
- 593 Aplin, A.C. and Yagiz, J.H., 2011. Mudstone diversity: Origin and implications for source, seal, and reservoir
594 properties in petroleum systems. AAPG bulletin, 95(12), pp.2031-2059.
- 595 Aplin, A.C., Matenaar, I.F. and van der Pluijm, B., 2003. Influence of mechanical compaction and chemical
596 diagenesis on the microfabric and fluid flow properties of Gulf of Mexico mudstones. Journal of Geochemical
597 Exploration, 78, pp.449-451.
- 598 Aplin, A.C., Matenaar, I.F., McCarty, D.K. and van Der Pluijm, B.A., 2006. Influence of mechanical compaction
599 and clay mineral diagenesis on the microfabric and pore-scale properties of deep-water Gulf of Mexico
600 mudstones. Clays and Clay Minerals, 54(4), pp.500-514.



- 601 Backman, J., W. Chen, S. Kachovich, F. L. Mitchison, K. E. Petronotis, T. Yang and X. Zhao (2019). Data report;
602 Revised age models for IODP Sites U1480 and U1481, Expedition 362. Proceedings of the International Ocean
603 Discovery Program, Expedition Reports 362: 7.
- 604 Bennett, R.H., Bryant, W.R. and Keller, G.H., 1981. Clay fabric of selected submarine sediments; fundamental
605 properties and models. *Journal of Sedimentary Research*, 51(1), pp.217-232.
- 606 Bennett, R.H., O'Brien, N.R. and Hulbert, M.H., 1991. Determinants of clay and shale microfabric signatures:
607 processes and mechanisms. In *Microstructure of Fine-Grained Sediments* (pp. 5-32). Springer, New York, NY.
- 608 ~~Bjørlykke, K. and Hoeg, K., 1997. Effects of burial diagenesis on stresses, compaction and fluid flow in
609 sedimentary basins. *Marine and Petroleum Geology*, 14(3), pp.267-276.~~
- 610 ~~Bjørlykke, K., 1998. Clay mineral diagenesis in sedimentary basins-a key to the prediction of rock properties.
611 Examples from the North Sea Basin. *Clay minerals*, 33(1), pp.15-34.~~
- 612 Blenkinsop, T.G., 2007. Deformation microstructures and mechanisms in minerals and rocks. Springer Science &
613 Business Media.
- 614 ~~Boisson, J.Y. (2005). *Clay Club Catalogue of Characteristics of Argillaceous Rocks* (OECD NEA No. 4436).~~
- 615 Borradaile, G.J., 1981. Particulate flow of rock and the formation of cleavage. *Tectonophysics*, 72(3-4), pp.305-
616 321.
- 617 Bowles, F.A., Bryant, W.R. and Wallin, C., 1969. Microstructure of unconsolidated and consolidated marine
618 sediments. *Journal of Sedimentary Research*, 39(4), pp.1546-1551.
- 619 Bray, C.J. and Karig, D.E., 1985. Porosity of sediments in accretionary prisms and some implications for
620 dewatering processes. *Journal of Geophysical Research: Solid Earth*, 90(B1), pp.768-778.
- 621 ~~Casagrande, A., 1932. Research on the Atterberg limits of soils. *Public roads*, 13(8), pp.121-136.~~
- 622 ~~Casagrande, A., 1932. The structure of clay and its importance in foundation engineering. *Boston Society Civil
623 Engineers Journal*.~~
- 624 ~~Cetin, H., 2004. Soil-particle and pore orientations during consolidation of cohesive soils. *Engineering
625 geology*, 73(1-2), pp.1-11.~~
- 626 Chester, F.M., Rowe, C., Ujiie, K., Kirkpatrick, J., Regalla, C., Remitti, F., Moore, J.C., Toy, V., Wolfson-
627 Schwehr, M., Bose, S. and Kameda, J., 2013. Structure and composition of the plate-boundary slip zone for the
628 2011 Tohoku-Oki earthquake. *Science*, 342(6163), pp.1208-1211.



- 629 ~~Collins, K.T. and McGown, A., 1974. The form and function of microfabric features in a variety of natural~~
630 ~~soils. *Geotechnique*, 24(2), pp.223-254.~~
- 631 ~~Cook, B.J., Henstock, T.J., McNeill, L.C. and Bull, J.M., 2014. Controls on spatial and temporal evolution of~~
632 ~~prism faulting and relationships to plate boundary slip offshore north-central Sumatra. *Journal of Geophysical*~~
633 ~~*Research: Solid Earth*, 119(7), pp.5594-5612.~~
- 634 ~~Cubas, N., Souloumiac, P. and Singh, S.C., 2016. Relationship link between landward vergence in accretionary~~
635 ~~prisms and tsunami generation. *Geology*, 44(10), pp.787-790.~~
- 636 ~~Curtis, C.D., Lipshie, S.R., Oertel, G. and Pearson, M.J., 1980. Clay orientation in some Upper Carboniferous~~
637 ~~mudrocks, its relationship to quartz content and some inferences about fissility, porosity and compactional~~
638 ~~history. *Sedimentology*, 27(3), pp.333-339.~~
- 639 Day-Stirrat, R.J., Aplin, A.C., Środoń, J. and Van der Pluijm, B.A., 2008. Diagenetic reorientation of phyllosilicate
640 minerals in Paleogene mudstones of the Podhale Basin, southern Poland. *Clays and Clay Minerals*, 56(1), pp.100-
641 111.
- 642 Day-Stirrat, R.J., Flemings, P.B., You, Y., Aplin, A.C. and van der Pluijm, B.A., 2012. The fabric of consolidation
643 in Gulf of Mexico mudstones. *Marine Geology*, 295, pp.77-85.
- 644 Day-Stirrat, R.J., Milliken, K.L., Dutton, S.P., Loucks, R.G., Hillier, S., Aplin, A.C. and Schleicher, A.M., 2010.
645 Open-system chemical behavior in deep Wilcox Group mudstones, Texas Gulf Coast, USA. *Marine and Petroleum*
646 *Geology*, 27(9), pp.1804-1818.
- 647 Dean, S.M., McNeill, L.C., Henstock, T.J., Bull, J.M., Gulick, S.P., Austin, J.A., Bangs, N.L., Djajadihardja, Y.S.
648 and Permana, H., 2010. Contrasting décollement and prism properties over the Sumatra 2004–2005 earthquake
649 rupture boundary. *Science*, 329(5988), pp.207-210.
- 650 **Den H.**, S.A. and Spiers, C.J., 2014. A microphysical model for fault gouge friction applied to subduction
651 megathrusts. *Journal of Geophysical Research: Solid Earth*, 119(2), pp.1510-1529.
- 652 Desbois, G., Höhne, N., Urai, J.L., Bésuelle, P. and Viggiani, G., 2017. Deformation in cemented mudrock
653 (Callovo–Oxfordian Clay) by microcracking, granular flow and phyllosilicate plasticity: insights from triaxial
654 deformation, broad ion beam polishing and scanning electron microscopy. *Solid Earth*, 8(2), pp.291-305.
- 655 ~~Desbois, G., Urai, J.L. and Kukla, P.A., 2009a. Morphology of the pore space in claystones: evidence from~~
656 ~~BIB/FIB ion beam sectioning and cryo-SEM observations. *eEarth Discussions*, 4(1), pp.1-19.~~
- 657 Desbois, G., Urai, J.L., Kukla, P.A., Konstanty, J. and Baerle, C., 2011. High-resolution 3D fabric and porosity
658 model in a tight gas sandstone reservoir: A new approach to investigate microstructures from mm-to nm-scale
659 combining argon beam cross-sectioning and SEM imaging. *Journal of Petroleum Science and Engineering*, 78(2),
660 pp.243-257.



- 661 ~~Desbois, G., Urai, J.L. and Kukla, P.A., 2009b. Morphology of the pore space in claystones: evidence from~~
662 ~~BIB/FIB ion beam sectioning and cryo-SEM observations. *eEarth Discussions*, 4(1), pp.1-19.~~
- 663 ~~Desbois, G., Urai, J.L., Hemes, S., Brassinnes, S., De Craen, M. and Sillen, X., 2014. Nanometer-scale pore fluid~~
664 ~~distribution and drying damage in preserved clay cores from Belgian clay formations inferred by BIB-cryo-~~
665 ~~SEM. *Engineering Geology*, 179, pp.117-131.~~
- 666 ~~Desbois, G., Urai, J.L., Hemes, S., Brassinnes, S., De Craen, M. and Sillen, X., 2014. Nanometer-scale pore fluid~~
667 ~~distribution and drying damage in preserved clay cores from Belgian clay formations inferred by BIB-cryo-~~
668 ~~SEM. *Engineering Geology*, 179, pp.117-131.~~
- 669 ~~Díaz-Azpiroz, M., Brune, S., Leever, K.A., Fernández, C. and Czeck, D.M., 2016. Tectonics of oblique plate~~
670 ~~boundary systems. *Tectonophysics*, 693, pp.165-170.~~
- 671 ~~Djéran-Maigre, I., Tessier, D., Grunberger, D., Velde, B. and Vasseur, G., 1998. Evolution of microstructures and~~
672 ~~of macroscopic properties of some clays during experimental compaction. *Marine and Petroleum Geology*, 15(2),~~
673 ~~pp.109-128.~~
- 674 ~~Djéran-Maigre, I., Tessier, D., Grunberger, D., Velde, B. and Vasseur, G., 1998. Evolution of microstructures and~~
675 ~~of macroscopic properties of some clays during experimental compaction. *Marine and Petroleum Geology*, 15(2),~~
676 ~~pp.109-128.~~
- 677 ~~Dugan, B., McNeill, L. and Petronotis, K., 2017. Expedition 362 preliminary report: Sumatra subduction~~
678 ~~zone. International Ocean Discovery Program.~~
- 679 ~~Dutilleul, J., Bourlange, S., Conin, M. and Géraud, Y., 2020. Quantification of bound water content, interstitial~~
680 ~~porosity and fracture porosity in the sediments entering the North Sumatra subduction zone from Cation Exchange~~
681 ~~Capacity and IODP Expedition 362 resistivity data. *Marine and Petroleum Geology*, 111, pp.156-165.~~
- 682 ~~Dutta, N.C., 1986. Shale compaction, burial diagenesis, and geopressures: A dynamic model, solution and some~~
683 ~~results. *Collection colloques et séminaires-Institut français du pétrole*, (44), pp.149-172.~~
- 684 ~~Ehrenberg, S. N. 1989. Assessing the relative importance of compaction processes and cementation to reduction~~
685 ~~of porosity in sandstones: discussion. *American Association of Petroleum Geologists Bulletin* 73: 1274-1276.~~
- 686 ~~Emmanuel, S. and Day-Stirrat, R.J., 2012. A framework for quantifying size dependent deformation of nano-scale~~
687 ~~pores in mudrocks. *Journal of applied geophysics*, 86, pp.29-35.~~
- 688 ~~Fawad, M., Mondol, N.H., Jahren, J. and Bjørlykke, K., 2010. Microfabric and rock properties of experimentally~~
689 ~~compressed silt-clay mixtures. *Marine and Petroleum Geology*, 27(8), pp.1698-1712.~~
- 690 ~~Fernandez-Blanco, D., Philippon, M. and von Hagke, C., 2016. Structure and kinematics of the Sumatran fault~~
691 ~~system in North Sumatra (Indonesia). *Tectonophysics*, 693, pp.453-464.~~



- 692 Fossen, H., 2016. Structural geology. Cambridge university press.
- 693 ~~Geersen, J., McNeill, L., Henstock, T.J. and Gaedicke, C., 2013. The 2004 Aceh-Andaman Earthquake: Early clay~~
694 ~~dehydration controls shallow seismic rupture. *Geochemistry, Geophysics, Geosystems*, 14(9), pp.3315-3323.~~
- 695 Ghosal, D., Singh, S.C. and Martin, J., 2014. Shallow subsurface morphotectonics of the NW Sumatra subduction
696 system using an integrated seismic imaging technique. *Geophysical Journal International*, 198(3), pp.1818-1831.
- 697 ~~Gulick, S.P., Austin, J.A., McNeill, L.C., Bangs, N.L., Martin, K.M., Henstock, T.J., Bull, J.M., Dean, S.,~~
698 ~~Djajadihardja, Y.S. and Permana, H., 2011. Updip rupture of the 2004 Sumatra earthquake extended by thick~~
699 ~~indurated sediments. *Nature Geoscience*, 4(7), pp.453-456.~~
- 700 ~~Guo, P. and Stolle, D.F.E., 2013. Coupled analysis of bifurcation and shear band in saturated soils. *Soils and*~~
701 ~~foundations, 53(4), pp.525-539.~~
- 702 ~~Handy, M.R., 1994. Flow laws for rocks containing two non-linear viscous phases: a phenomenological~~
703 ~~approach. *Journal of Structural Geology*, 16(3), pp.287-301.~~
- 704 Hemes, S., Desbois, G., Klaver, J. and Urai, J.L., 2016. Microstructural characterisation of the Ypresian clays
705 (Kallo-1) at nanometre resolution, using broad-ion beam milling and scanning electron microscopy. *Netherlands*
706 *Journal of Geosciences*, 95(3), pp.293-313.
- 707 ~~Hemes, S., Desbois, G., Urai, J.L., De Craen, M. and Honty, M., 2013. Variations in the morphology of porosity~~
708 ~~in the Boom Clay Formation: insights from 2D high resolution BIB-SEM imaging and Mercury injection~~
709 ~~Porosimetry. *Netherlands Journal of geosciences*, 92(4), pp.275-300.~~
- 710 Hemes, S., Desbois, G., Urai, J.L., De Craen, M. and Honty, M., 2013. Variations in the morphology of porosity
711 in the Boom Clay Formation: insights from 2D high resolution BIB-SEM imaging and Mercury injection
712 Porosimetry. *Netherlands Journal of geosciences*, 92(4), pp.275-300.
- 713 Hemes, S., Desbois, G., Urai, J.L., Schröppel, B. and Schwarz, J.O., 2015. Multi-scale characterization of porosity
714 in Boom Clay (HADES-level, Mol, Belgium) using a combination of X-ray μ -CT, 2D BIB-SEM and FIB-SEM
715 tomography. *Microporous and mesoporous materials*, 208, pp.1-20.
- 716 Hesse, R., 1975. Turbiditic and non-turbiditic mudstone of Cretaceous flysch sections of the East Alps and other
717 basins. *Sedimentology*, 22(3), pp.387-416.
- 718 Hippchen, S. and Hyndman, R.D., 2008. Thermal and structural models of the Sumatra subduction zone:
719 Implications for the megathrust seismogenic zone. *Journal of Geophysical Research: Solid Earth*, 113(B12).
- 720 Ho, N.C., Peacor, D.R. and Van der Pluijm, B.A., 1999. Preferred orientation of phyllosilicates in Gulf Coast
721 mudstones and relation to the smectite-illite transition. *Clays and Clay Minerals*, 47(4), pp.495-504.



- 722 ~~Houben, M.E., Desbois, G. and Urai, J.L., 2013. Pore morphology and distribution in the Shaly facies of Opalinus~~
723 ~~Clay (Mont Terri, Switzerland): Insights from representative 2D BIB-SEM investigations on mm to nm~~
724 ~~scale. Applied Clay Science, 71, pp.82-97.~~
- 725 Houben, M.E., Desbois, G. and Urai, J.L., 2014. A comparative study of representative 2D microstructures in
726 Shaly and Sandy facies of Opalinus Clay (Mont Terri, Switzerland) inferred from BIB-SEM and MIP
727 methods. Marine and Petroleum Geology, 49, pp.143-161.
- 728 ~~Hunze, S. and Wonik, T., 2007. Compaction in the Nankai and Barbados accretionary prisms: New insights from~~
729 ~~logging-while-drilling data. Geochemistry, Geophysics, Geosystems, 8(2).~~
- 730 Hüpers, A., Ikari, M.J., Dugan, B., Underwood, M.B. and Kopf, A.J., 2015. Origin of a zone of anomalously high
731 porosity in the subduction inputs to Nankai Trough. Marine Geology, 361, pp.147-162.
- 732 Hüpers, A., Torres, M.E., Owari, S., McNeill, L.C., Dugan, B., Henstock, T.J., Milliken, K.L., Petronotis, K.E.,
733 Backman, J., Bourlange, S. and Chemale, F., 2017. Release of mineral-bound water prior to subduction tied to
734 shallow seismogenic slip off Sumatra. Science, 356(6340), pp.841-844.
- 735 ~~Ikari, M.J., Niemeijer, A.R. and Marone, C., 2015. Experimental investigation of incipient shear failure in foliated~~
736 ~~rock. Journal of Structural Geology, 77, pp.82-91.~~
- 737 ~~Illangasekare, T., Tyler, S.W., Clement, T.P., Villholth, K.G., Perera, A.P.G.R.L., Obeysekera, J., Gunatilaka, A.,~~
738 ~~Panabokke, C.R., Hyndman, D.W., Cunningham, K.J. and Kaluarachchi, J.J., 2006. Impacts of the 2004 tsunami~~
739 ~~on groundwater resources in Sri Lanka. Water Resources Research, 42(5).~~
- 740 ~~Ingram, G.M. and Urai, J.L., 1999. Top-seal leakage through faults and fractures: the role of mudrock~~
741 ~~properties. Geological Society, London, Special Publications, 158(1), pp.125-135.~~
- 742 ~~Jacob, G., Kisch, H.J. and van der Pluijm, B.A., 2000. The relationship of phyllosilicate orientation, X-ray~~
743 ~~diffraction intensity ratios, and c/b fissility ratios in metasedimentary rocks of the Helvetic zone of the Swiss Alps~~
744 ~~and the Caledonides of Jaemtland, central western Sweden. Journal of Structural Geology, 22(2), pp.245-258.~~
- 745 ~~Jessell, M.W., Bons, P.D., Griera, A., Evans, L.A. and Wilson, C.J., 2009. A tale of two viscosities. Journal of~~
746 ~~Structural Geology, 31(7), pp.719-736.~~
- 747 Jiang, M., Klaver, J., Schmatz, J. and Urai, J.L., 2015. Nanoscale porosity analysis in geological materials. Acta
748 Stereologica.
- 749 Kameda, A., Dvorkin, J., Keehm, Y., Nur, A. and Bosl, W., 2006. Permeability-porosity transforms from small
750 sandstone fragments. Geophysics, 71(1), pp.N11-N19.
- 751 Karaborni, S., Smit, B., Heidug, W., Urai, J. and Van Oort, E., 1996. The swelling of clays: molecular simulations
752 of the hydration of montmorillonite. Science, 271(5252), pp.1102-1104.



- 753 Klaver, J., Desbois, G., Littke, R. and Urai, J.L., 2015. ~~BIB-SEM characterization of pore space morphology and~~
754 ~~distribution in postmature to overmature samples from the Haynesville and Bossier Shales. Marine and petroleum~~
755 ~~Geology, 59, pp.451-466.~~
- 756 Klaver, J., Desbois, G., Littke, R. and Urai, J.L., 2016. BIB-SEM pore characterization of mature and post mature
757 Posidonia Shale samples from the Hils area, Germany. International Journal of Coal Geology, 158, pp.78-89.
- 758 Klaver, J., Desbois, G., Urai, J.L. and Littke, R., 2012. ~~BIB-SEM study of the pore space morphology in early~~
759 ~~mature Posidonia Shale from the Hils area, Germany. International Journal of Coal Geology, 103, pp.12-25.~~
- 760 Klaver, J., Desbois, G., Urai, J.L. and Littke, R., 2012. BIB-SEM study of the pore space morphology in early
761 mature Posidonia Shale from the Hils area, Germany. International Journal of Coal Geology, 103, pp.12-25.
- 762 Klaver, J., Hemes, S., Houben, M., Desbois, G., Radi, Z. and Urai, J.L., 2015. ~~The connectivity of pore space in~~
763 ~~mudstones: insights from high-pressure Wood's metal injection, BIB-SEM imaging, and mercury intrusion~~
764 ~~porosimetry. Geofluids, 15(4), pp.577-591.~~
- 765 Klaver, J., Hemes, S., Houben, M., Desbois, G., Radi, Z. and Urai, J.L., 2015. ~~The connectivity of pore space in~~
766 ~~mudstones: insights from high-pressure Wood's metal injection, BIB-SEM imaging, and mercury intrusion~~
767 ~~porosimetry. Geofluids, 15(4), pp.577-591.~~
- 768 Klinkenberg, M., Kaufhold, S., Dohrmann, R. and Siegesmund, S., 2009. ~~Influence of carbonate microfibrils on~~
769 ~~the failure strength of claystones. Engineering Geology, 107(1-2), pp.42-54.~~
- 770 Kooi, H., 1997. ~~Insufficiency of compaction disequilibrium as the sole cause of high pore fluid pressures in pre-~~
771 ~~Cenozoic sediments. Basin Research, 9(3), pp.227-241.~~
- 772 Kuila, U. and Prasad, M., 2013. Specific surface area and pore-size distribution in clays and shales. Geophysical
773 Prospecting, 61(2-Rock Physics for Reservoir Exploration, Characterisation and Monitoring), pp.341-362.
- 774 Kuncoro, A.K., Cubas, N., Singh, S.C., Etchebes, M. and Tapponnier, P., 2015. ~~Tsunamigenic potential due to~~
775 ~~frontal rupturing in the Sumatra locked zone. Earth and Planetary Science Letters, 432, pp.311-322.~~
- 776 Lahann, R., Huffman, A.R. and Bowers, G.L., 2002. ~~Impact of smectite diagenesis on compaction modeling and~~
777 ~~compaction equilibrium. MEMOIRS AMERICAN ASSOCIATION OF PETROLEUM GEOLOGISTS, pp.61-~~
778 ~~72.~~
- 779 Lambe, T.W., 1953, October. ~~The structure of inorganic soil. In Proceedings of the American Society of Civil~~
780 ~~Engineers (Vol. 79, No. 10, pp. 1-49). ASCE.~~
- 781 Lambe, T.W., 1958. ~~The structure of compacted clays. Journal of the Soil Mechanics and Foundations~~
782 ~~Division, 84(2), pp.1654-1.~~



- 783 Lander, R. H. and O. Walderhaug 1999. Predicting porosity through simulating sandstone compaction and quartz
784 cementation. American Association of Petroleum Geologists Bulletin 83: 433-449.
- 785 Lander, R. H., R. H. Larese and L. M. Bonnell 2008. Toward more accurate quartz cement models: The importance
786 of euhedral versus noneuhedral growth rates. American Association Petroleum Geologists Bulletin 92: 1537-1563.
- ~~787 Laurich, B., Urai, J.L. and Nussbaum, C., 2017. Microstructures and deformation mechanisms in Opalinus Clay:
788 Insights from scaly clay from the Main Fault in the Mont Terri Rock Laboratory (CH). Solid Earth, 8(1), pp.27-
789 44.~~
- 790 Laurich, B., Urai, J.L., Desbois, G., Vollmer, C. and Nussbaum, C., 2014. Microstructural evolution of an incipient
791 fault zone in Opalinus Clay: Insights from an optical and electron microscopic study of ion-beam polished samples
792 from the Main Fault in the Mt-Terri Underground Research Laboratory. Journal of Structural Geology, 67, pp.107-
793 128.
- ~~794 Lay, T., Ammon, C.J., Kanamori, H., Yamazaki, Y., Cheung, K.F. and Hutko, A.R., 2011. The 25 October 2010
795 Mentawai tsunami earthquake (Mw 7.8) and the tsunami hazard presented by shallow megathrust
796 ruptures. Geophysical Research Letters, 38(6).~~
- 797 Lay, T., Kanamori, H., Ammon, C.J., Nettles, M., Ward, S.N., Aster, R.C., Beck, S.L., Bilek, S.L., Brudzinski,
798 M.R., Butler, R. and DeShon, H.R., 2005. The great Sumatra-Andaman earthquake of 26 december
799 2004. science, 308(5725), pp.1127-1133.
- 800 Lazar, O.R., Bohacs, K.M., Macquaker, J.H., Schieber, J. and Demko, T.M., 2015. Capturing key attributes of
801 fine-grained sedimentary rocks in outcrops, cores, and thin sections: nomenclature and description
802 guidelines. Journal of Sedimentary Research, 85(3), pp.230-246.
- ~~803 Li, Z. and J. Schieber 2018. Composite particles in mudstones: Examples from the Late Cretaceous Tununk shale
804 member of the Mancos Shale Formation. Journal of Sedimentary Research 8812: 1319-1344. Lithic grains in shale~~
- ~~805 Li, Z., J. Schieber and P. K. Pedersen 2021. On the origin and significance of composite particles in mudstones;
806 examples from the Cenomanian Dunvegan Formation. Sedimentology 682: 737-754. Lithic grains in shale~~
- ~~807 Logan, J.M. and Rauenzahn, K.A., 1987. Frictional dependence of gouge mixtures of quartz and montmorillonite
808 on velocity, composition and fabric. Tectonophysics, 144(1-3), pp.87-108.~~
- ~~809 Lu, J., K. L. Milliken and R. M. Reed 2011. Diagenesis and sealing capacity of the Middle Tuscaloosa mudstone
810 at the Cranfield CO2 injection site, Mississippi, USA. Environmental Geosciences 3: 35-53.~~
- 811 Lundegard, P. D. 1992. Sandstone porosity loss--a 'big picture' view of the importance of compaction. Journal of
812 Sedimentary Petrology 62: 250-260.



- 813 ~~Lupini, J.F., Skinner, A.E. and Vaughan, P.R., 1981. The drained residual strength of cohesive~~
814 ~~soils. *Geotechnique*, 31(2), pp.181-213.~~
- 815 ~~Mandelbrot, B.B., Pfeifer, P., Biham, O., Malcai, O., Lidar, D. and Avnir, D., 1998. Is nature~~
816 ~~fractal?. *Science*, 279(5352), pp.783-783.~~
- 817 ~~March, A., 1932. Mathematische Theorie der Regelung nach der Korngestalt bei affiner Deformation: *Zeitschrift*~~
818 ~~für Kristallographie, v. 81.~~
- 819 ~~McNeill, L.C. and Henstock, T.J., 2014. Forearc structure and morphology along the Sumatra-Andaman~~
820 ~~subduction zone. *Tectonics*, 33(2), pp.112-134.~~
- 821 McNeill, L.C., Dugan, B. and Petronotis, K.E., The Expedition 362 Scientists (2017). Sumatra Subduction
822 Zone. Proceedings of the International Ocean Discovery Program, 362.
- 823 Meade, R.H., 1964. Removal of water and rearrangement of particles during the compaction of clayey sediments.
824 US Government Printing Office.
- 825 ~~Miller, S.A., 2013. The role of fluids in tectonic and earthquake processes. In *Advances in geophysics* (Vol. 54,~~
826 ~~pp. 1-46). Elsevier.~~
- 827 Milliken K. L. 2019. Compactional and mass-balance constraints inferred from the volume of quartz cementation
828 in mudrocks. *Mudstone Diagenesis: New Research Perspectives for Shale Hydrocarbon Reservoirs, Seals, and*
829 *Source Rocks*. AAPG. 120: 33-48.
- 830 Milliken, K. L. 2014. A compositional classification for grain assemblages in fine-grained sediments and
831 sedimentary rocks. *Journal of Sedimentary Research* 84: 1185-1199.
- 832 ~~Milliken, K. L. and M. E. Curtis 2016. Imaging pores in sedimentary rocks: Foundation of porosity prediction.~~
833 ~~*Marine and Petroleum Geology* 73: 590-608.~~
- 834 Milliken, K. L. and R. J. Day-Stirrat 2013. Cementation in mudrocks: Brief review with examples from cratonic
835 basin mudrocks. *Memoir. J.-Y. Chatellier*. Tulsa, Oklahoma, USA, AAPG: in press.
- 836 Milliken, K. L. and T. Olson 2017. Silica diagenesis, porosity evolution, and mechanical behavior in siliceous
837 mudstones, Mowry Shale Cretaceous, Rocky Mountains, U.S.A. *Journal of Sedimentary Research* 87: 366-387.
- 838 Milliken, K. L., M. Rudnicki, D. N. Awwiller and T. Zhang 2013. Organic matter-hosted pore system, Marcellus
839 Formation Devonian, Pennsylvania, USA. *AAPG Bulletin* 97: 177-200.
- 840 Milliken, K. L., W. L. Esch, R. M. Reed and T. Zhang 2012. Grain assemblages and strong diagenetic overprinting
841 in siliceous mudrocks, Barnett Shale Mississippian, Fort Worth Basin, Texas, U.S.A. *AAPG Bulletin* 96: 1553-
842 1578.



- 843 Milliken, K., and Olson, T., 2016, Amorphous and crystalline solids as artifacts in SEM images, in Olson, T.,
844 Imaging Unconventional Reservoir Pore Systems: AAPG Memoir, v. 112, p. 1-8,
845 <http://doi.org/10.1306/13592013M112252>.
- ~~846 Milliken, K.L. and Hayman, N.W., 2019. Mudrock components and the genesis of bulk rock properties: review of
847 current advances and challenges. Shale: Subsurface Science and Engineering, pp.1-25.~~
- 848 Mitchell, J.K., 1956. The fabric of natural clays and its relation to engineering properties. In Highway Research
849 Board Proceedings (Vol. 35).
- ~~850 Moeremans, R., Singh, S.C., Mukti, M., McArdle, J. and Johansen, K., 2014. Seismic images of structural
851 variations along the deformation front of the Andaman-Sumatra subduction zone: implications for rupture
852 propagation and tsunamigenesis. Earth and Planetary Science Letters, 386, pp.75-85.~~
- ~~853 Moeremans, R.E. and Singh, S.C., 2014. Seismic evidence of continental margin influence on the NinetyEast
854 Ridge in the Bay of Bengal. Geophysical Research Letters, 41(20), pp.7143-7150.~~
- 855 Moeremans, R.E. and Singh, S.C., 2015. Fore-arc basin deformation in the Andaman-Nicobar segment of the
856 Sumatra-Andaman subduction zone: Insight from high-resolution seismic reflection data. Tectonics, 34(8),
857 pp.1736-1750.
- 858 Mondol, N.H., Bjørlykke, K., Jahren, J. and Høeg, K., 2007. Experimental mechanical compaction of clay mineral
859 aggregates—Changes in physical properties of mudstones during burial. Marine and petroleum geology, 24(5),
860 pp.289-311.
- ~~861 Moon, C.F., 1972. The microstructure of clay sediments. Earth Science Reviews, 8(3), pp.303-321.~~
- ~~862 Moore, D.E. and Lockner, D.A., 2004. Crystallographic controls on the frictional behavior of dry and water-
863 saturated sheet structure minerals. Journal of Geophysical Research: Solid Earth, 109(B3).~~
- ~~864 Moore, D.M. and R. C. Reynolds, Jr. (1989). X-ray diffraction and the identification and analysis of clay minerals.
865 United States, Oxford Univ. Press : New York, NY, 332 p. Morgenstern, N.R. and Tchalenko, J.S., 1967.
866 Microscopic structures in kaolin subjected to direct shear. Geotechnique, 17(4), pp.309-328.~~
- 867 Morgenstern, N.R. and Tchalenko, J.S., 1967. Microscopic structures in kaolin subjected to direct
868 shear. Geotechnique, 17(4), pp.309-328.
- 869 Nakano, R., 1967. On weathering and change of properties of tertiary mudstone related to landslide. Soils and
870 Foundations, 7(1), pp.1-14.
- 871 Neagu, R.C., Cartwright, J. and Davies, R., 2010. Measurement of diagenetic compaction strain from quantitative
872 analysis of fault plane dip. Journal of Structural Geology, 32(5), pp.641-655.



- 873 Oertel, G. and Curtis, C.D., 1972. Clay-ironstone concretion preserving fabrics due to progressive
874 compaction. *Geological Society of America Bulletin*, 83(9), pp.2597-2606.
- 875 Paxton, S. T., J. O. Szabo, J. M. Adjukiewicz and R. E. Klimentidis 2002. Construction of an intergranular volume
876 compaction curve for evaluating and predicting compaction and porosity loss in rigid-grain sandstone reservoirs.
877 *American Association of Petroleum Geologists Bulletin* 86: 2047-2067.
- 878 Pickering, K. T., H. Pouderoux, L. C. McNeill, J. Backman, F. Chemale, S. Kutterolf, K. L. Milliken, H.
879 Mukoyoshi, T. J. Henstock, D. E. Stevens, C. Parnell and B. Dugan, 2020. Sedimentology, stratigraphy and
880 architecture of the Nicobar Fan (BengalNicobar Fan System), Indian Ocean: Results from International Ocean
881 Discovery Program Expedition 362. *Sedimentology* 67(5): 2248-2281.
- 882 ~~Philipp, T., Amann-Hildenbrand, A., Laurich, B., Desbois, G., Littke, R. and Urai, J.L., 2017. The effect of
883 microstructural heterogeneity on pore size distribution and permeability in Opalinus Clay (Mont Terri,
884 Switzerland): insights from an integrated study of laboratory fluid flow and pore morphology from BIB-SEM
885 images. *Geological Society, London, Special Publications*, 454(1), pp.85-106.~~
- 886 Pommer, M. E. and K. L. Milliken 2015. Pore types and pore-size distributions across thermal maturity, Eagle
887 Ford Formation, South Texas. *AAPG Bulletin* 99: 1713-1744.
- 888 ~~Porter, J.R., Knipe, R.J., Fisher, Q.J., Farmer, A.B., Allin, N.S., Jones, L.S., Palfrey, A.J., Garrett, S.W. and Lewis,
889 G., 2000. Deformation processes in the Britannia Field, UKCS. *Petroleum Geoscience*, 6(3), pp.241-254.~~
- 890 Prawirodirdjo, L., Bocl, Y., McCaffrey, R., Genrich, J., Calais, E., Stevens, C., Puntodewo, S.S.O., Subarya, C.,
891 Rais, J., Zwick, P. and Fauzi, R.M., 1997. Geodetic observations of interseismic strain segmentation at the Sumatra
892 subduction zone. *Geophysical research letters*, 24(21), pp.2601-2604.
- 893 ~~Proctor, B., Lockner, D.A., Kilgore, B.D., Mitchell, T.M. and Beeler, N.M., 2020. Direct evidence for fluid
894 pressure, dilatancy, and compaction affecting slip in isolated faults. *Geophysical Research Letters*, 47(16),
895 p.e2019GL086767.~~
- 896 ~~Rabinowitz, H.S., Savage, H.M., Skarbek, R.M., Ikari, M.J., Carpenter, B.M. and Collettini, C., 2018. Frictional
897 behavior of input sediments to the Hikurangi Trench, New Zealand. *Geochemistry, Geophysics,
898 Geosystems*, 19(9), pp.2973-2990.~~
- 899 Rosenberger, K., Underwood, M.B., Vrolijk, P. and Haines, S., 2020. Data report: clay mineral assemblages in
900 hemipelagic sediments entering the Sumatra subduction zone, IODP Sites U1480 and U1481, Expedition
901 362. Expedition, 362, p.1.
- 902 ~~Rubey, W.W. and King Hubbert, M., 1959. Role of fluid pressure in mechanics of overthrust faulting: II.
903 Overthrust belt in geosynclinal area of western Wyoming in light of fluid pressure hypothesis. *Geological Society
904 of America Bulletin*, 70(2), pp.167-206.~~



- 905 Rutter, E.H., Maddock, R.H., Hall, S.H. and White, S.H., 1986. Comparative microstructures of natural and
906 experimentally produced clay-bearing fault gouges. *Pure and applied geophysics*, 124(1), pp.3-30.
- 907 Rybacki, E., Morales, L.F.G., Naumann, M. and Dresen, G., 2014. Strain localization during high-temperature
908 creep of marble: The effect of inclusions. *Tectonophysics*, 634, pp.182-197.
- 909 Saffer, D.M. and Bekins, B.A., 2006. An evaluation of factors influencing pore pressure in accretionary complexes:
910 Implications for taper angle and wedge mechanics. *Journal of Geophysical Research: Solid Earth*, 111(B4).
- 911 Saito, S. and Goldberg, D., 2001. Compaction and dewatering processes of the oceanic sediments in the Costa
912 Rica and Barbados subduction zones: estimates from in situ physical property measurements. *Earth and Planetary
913 Science Letters*, 191(3-4), pp.283-293.
- 914 Salman, R., Lindsey, E.O., Feng, L., Bradley, K., Wei, S., Wang, T., Daryono, M.R. and Hill, E.M., 2020.
915 Structural controls on rupture extent of recent Sumatran Fault Zone earthquakes, Indonesia. *Journal of Geophysical
916 Research: Solid Earth*, 125(2), p.e2019JB018101.
- 917 Samsudin, M.S.F., Ariff, Z.M. and Ariffin, A., 2017, April. Deformation behavior of open-cell dry natural rubber
918 foam: Effect of different concentration of blowing agent and compression strain rate. In AIP Conference
919 Proceedings (Vol. 1835, No. 1, p. 020007). AIP Publishing LLC.
- 920 Schieber, J., 2016. Experimental testing of the transport durability of shale lithics and its implications for
921 interpreting the rock record. *Sedimentary Geology* 331: 162-169. Lithic grains in shale
- 922 Schieber, J., J. Southard and K. Thaisen 2007. Accretion of mudstone beds from migrating floccule ripples. *Science*
923 3185857: 1760-1763. Floccules in the range of sand-size.
- 924 Schmatz, J., Klaver, J., Jiang, M. and Urai, J.L., 2017. Nanoscale morphology of brine/oil/mineral contacts in
925 connected pores of carbonate reservoirs: Insights on wettability from Cryo-BIB-SEM. *SPE Journal*, 22(05),
926 pp.1374-1384.
- 927 Schneider, J., Flemings, P.B., Day-Stirrat, R.J. and Germaine, J.T., 2011. Insights into pore-scale controls on
928 mudstone permeability through resedimentation experiments. *Geology*, 39(11), pp.1011-1014.
- 929 Singh, S.C., Hananto, N., Mukti, M., Robinson, D.P., Das, S., Chauhan, A., Carton, H., Gratacos, B., Midnet, S.,
930 Djajadihardja, Y. and Harjono, H., 2011. Aseismic zone and earthquake segmentation associated with a deep
931 subducted seamount in Sumatra. *Nature Geoscience*, 4(5), pp.308-311.
- 932 Sintubin, M., 1994. Clay fabrics in relation to the burial history of shales. *Sedimentology*, 41(6), pp.1161-1169.
- 933 Terzaghi, K., 1925. Principles of soil mechanics: V — physical differences between sand and clay. *Engineering
934 News Record* 96, 912-915.



- 935 Terzaghi, K., Peck, R.B., 1948. Soil Mechanics In Engineering Practice. John Wiley and Sons, New York.
- 936 Torres, M. E. and K. Milliken (2019). Linked carbonate cementation and silicate dissolution in the sediments of
937 the Bengal-Nicobar Fan, inputs to the Sumatra subduction zone. prresAmerican Geophysical Union Fall Meeting
938 2019.
- 939 ~~Tunega, D. and Zaoui, A., 2020. Mechanical and bonding behaviors behind the bending mechanism of kaolinite
940 clay layers. The Journal of Physical Chemistry C, 124(13), pp.7432-7440.~~
- 941 Ukar, E. and Cloos, M., 2019. Cataclastic deformation and metasomatism in the subduction zone of mafic blocks-
942 in-mélange, San Simeon, California. Lithos, 346, p.105116.
- 943 ~~Van Olphen, H., 1964. Internal mutual flocculation in clay suspensions. Journal of Colloid Science, 19(4), pp.313-
944 322.~~
- 945 Vasseur, G., Djeran-Maigre, I., Grunberger, D., Rousset, G., Tessier, D. and Velde, B., 1995. Evolution of
946 structural and physical parameters of clays during experimental compaction. Marine and petroleum
947 geology, 12(8), pp.941-954.
- 948 Velde, B. 1996. Compaction trends of clay-rich deep sea sediments. Marine Geology 133(3-4): 193-201.
- 949 ~~Voltolini, M., Wenk, H.R., Mondol, N.H., Bjørlykke, K. and Jahren, J., 2009. Anisotropy of experimentally
950 compressed kaolinite-illite-quartz mixtures. Geophysics, 74(1), pp.D13-D23.~~
- 951 Vrolijk, P., 1990. On the mechanical role of smectite in subduction zones. Geology, 18(8), pp.703-707.
- 952 ~~Walker, K.T., Ishii, M. and Shearer, P.M., 2005. Rupture details of the 28 March 2005 Sumatra Mw 8.6 earthquake
953 imaged with teleseismic P waves. Geophysical Research Letters, 32(24).~~
- 954 Wang, X., Jiang, Z., Jiang, S., Chang, J., Zhu, L., Li, X. and Li, J., 2019. Full-scale pore structure and fractal
955 dimension of the Longmaxi shale from the Southern Sichuan Basin: Investigations using FE-SEM, gas adsorption
956 and mercury intrusion porosimetry. Minerals, 9(9), p.543.
- 957 ~~Wei, L.I., Jun, X.I.E., GAO, X.H., ZHANG, L.H. and Fang, Y.U., 2008. Characteristics of Jurassic mudstone
958 overpressure and its control on oil and gas accumulation in Turpan Depression. Petroleum Exploration and
959 Development, 35(1), pp.28-33.~~
- 960 Wenk, H.R., Voltolini, M., Kern, H., Popp, T. and Mazurek, M., 2008. Anisotropy in shale from Mont Terri. The
961 Leading Edge, 27(6), pp.742-748.
- 962 ~~Worden, R.H., Charpentier, D., Fisher, Q.J. and Aplin, A.C., 2005. Fabric development and the smectite to illite
963 transition in Upper Cretaceous mudstones from the North Sea: an image analysis approach. Geological Society,
964 London, Special Publications, 249(1), pp.103-114.~~



965 Yagiz, S., 2001. Overview of classification and engineering properties of shales for design considerations.
966 In Construction and Materials Issues 2001 (pp. 156-165).

967 ~~Yawar, Z. and J. Schieber 2017. On the origin of silt laminae in laminated shales. Sedimentary Geology 360: 22-~~
968 ~~34. Shows that coarse silt does segregates from clay in transport but fine silt is part of silt-clay floccules---hence~~
969 ~~floccules are bigger than fine silt size around 20-microns.~~

970 ~~Yong, R.N. and Sheeran, D.E., 1973. Fabric unit interaction and soil behaviour. In Proceedings International~~
971 ~~Symposium on Soil Structure.~~

972 Zakaria, Z., Mohamad Ariff, Z. and Abu Bakar, A., 2018. Monitoring deformation mechanism of foam cells in
973 polyethylene foams via optical microscopy: Effect of density and microstructure. Journal of Cellular
974 Plastics, 54(6), pp.957-976.

975 Zhou, J., Shrotriya, P. and Soboyejo, W.O., 2004. Mechanisms and mechanics of compressive deformation in
976 open-cell Al foams. Mechanics of Materials, 36(8), pp.781-797.

977

978

979

980

981

982

983

984

985

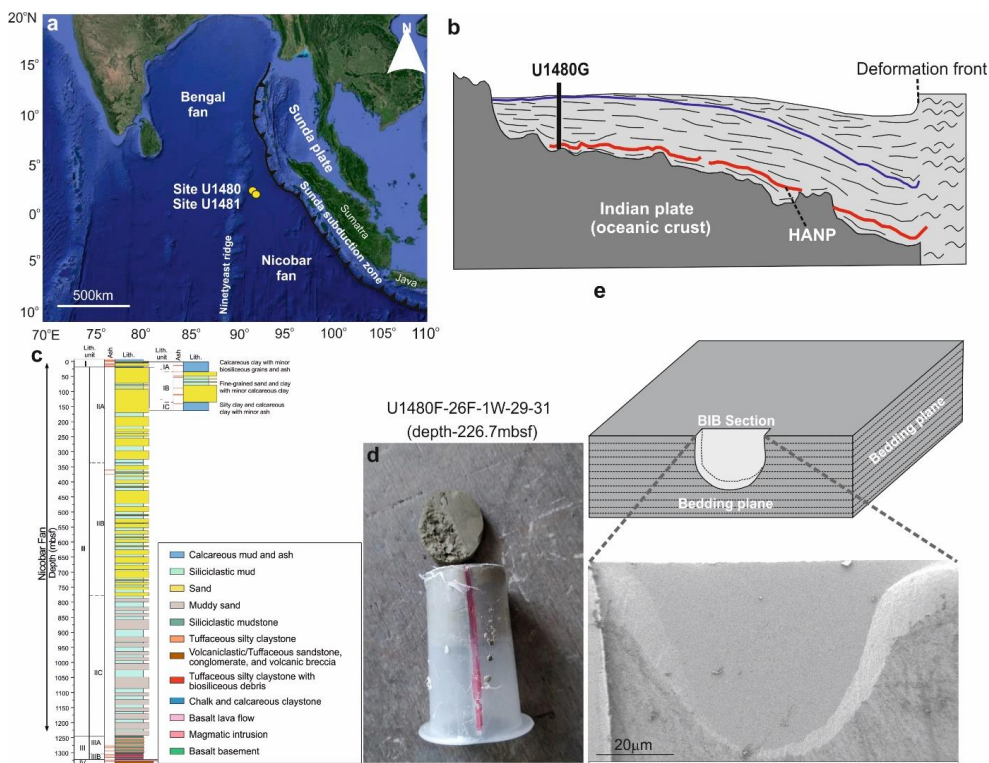
986

987

988

989

990



991

992 **Fig.1:** (a) Geological map of Sumatra subduction zone and location of U1480 and U1481 drilling sites (created
 993 from © Google Maps). (b) Location of drilling site U1480 in sectional view (adapted from seismic profile after
 994 Hüpers et al., 2017). (c) Lithostratigraphic units encountered at Site U1480 (adapted after McNeill et al., 2017).
 995 (d) Representative tube sample received from IODP repository, Japan. Red-colored line on tube surface represents
 996 notch used to denote orientation of samples collected from drill core. (e) Representative BIB cross-section polished
 997 perpendicular to bedding planes.

998

999

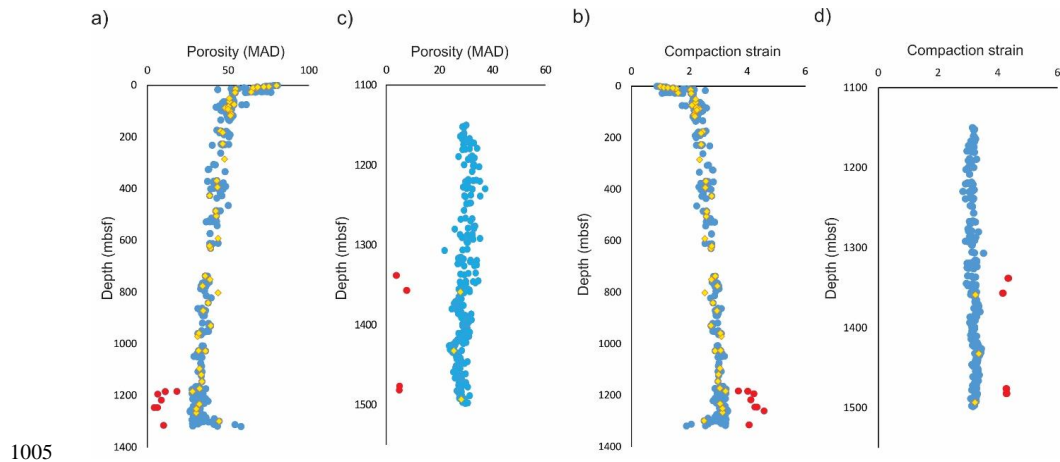
1000

1001

1002

1003

1004



1005

1006 **Fig.2:** (a) and (b) Shipboard MAD (Moisture and density) porosity vs depth data for mudstone samples recovered
1007 from Sites U1480 and U1481; (c) and (d) Cross-plot diagrams for estimated compaction strain vs depth
1008 corresponding to samples recovered from Sites U1480 and U1481. Yellow-colored symbols in (a), (b), (c), and (d)
1009 show 55 mud samples analyzed at RWTH-Aachen and BEG, Austin. Red-colored points are cemented (concretion)
1010 samples.

1011

1012

1013

1014

1015

1016

1017

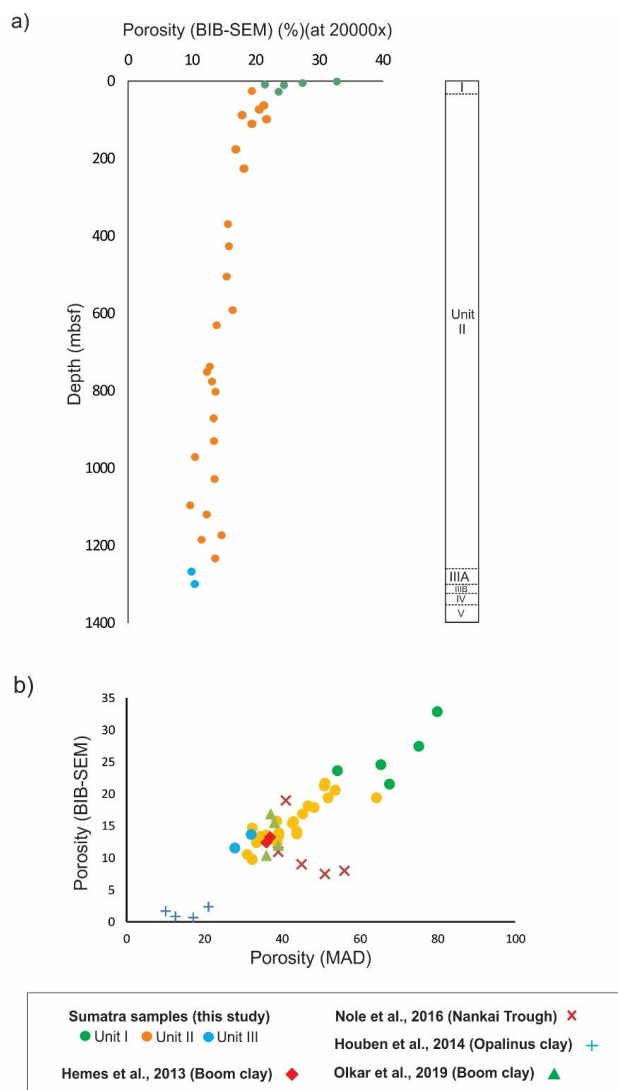
1018

1019

1020

1021

1022



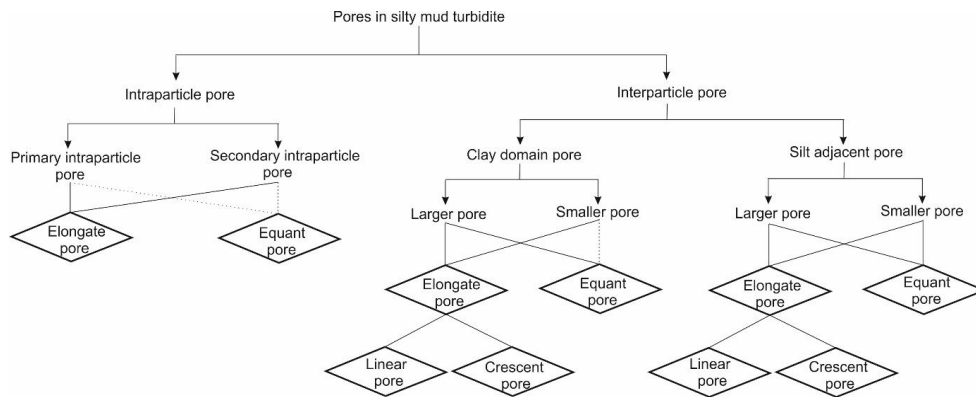
1023

1024 **Fig.3:** Porosity data for Units I (green dots), II (orange dots), and IIIA (blue dots). (a) BIB-SEM - depth plot. (b)
1025 BIB-SEM porosity vs MAD porosity. Note: linear relationship that intersects origin. The data estimated by Hemes
1026 et al., 2013; Houben et al., 2014; Olkar et al., 2019 also follow similar trend. However, the data estimated by Nole
1027 et al., 2016 is deviated from the general trend.

1028



1029



1030

1031

1032 **Fig.4:** Classification scheme adopted to demonstrate pore reduction mechanics with increasing compactional
1033 strain. Dashed lines indicate rare pore types.

1034

1035

1036

1037

1038

1039

1040

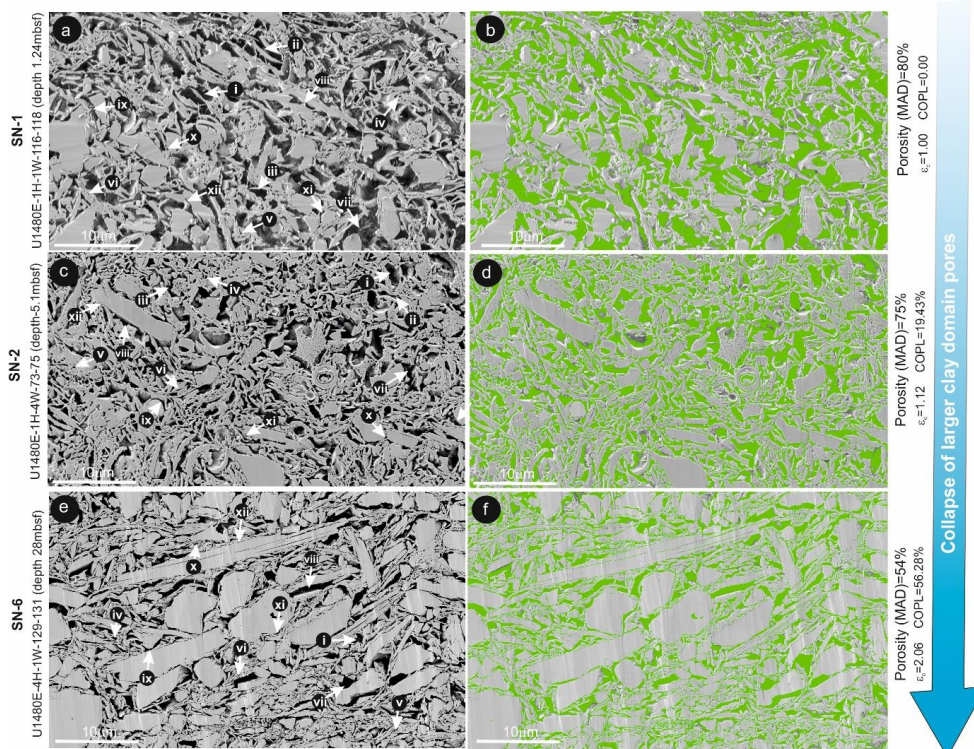
1041

1042

1043

1044

1045



1046

1047 **Fig.5:** Microstructural overview (BIB-SEM) of samples SN-1 (a and b), SN-2 (c and d), and SN-6 (e and f). Green
 1048 color represents segmented pores of the corresponding microstructure of sample. i = Equant large clay domain
 1049 pores, ii = elongated large clay domain pores, iii = Crescent-shaped large clay domain pores, iv = equant small
 1050 clay domain pores, v = Crescent-shaped small clay domain pores, vi = elongated small clay domain pores, vii =
 1051 Equant large silt-adjacent pores, viii = elongated large silt-adjacent pores, ix = Crescent-shaped large silt-adjacent
 1052 pores, x = equant small silt-adjacent pores, xi = Crescent-shaped small silt-adjacent pores, xii = elongated small
 1053 silt-adjacent pores.

1054

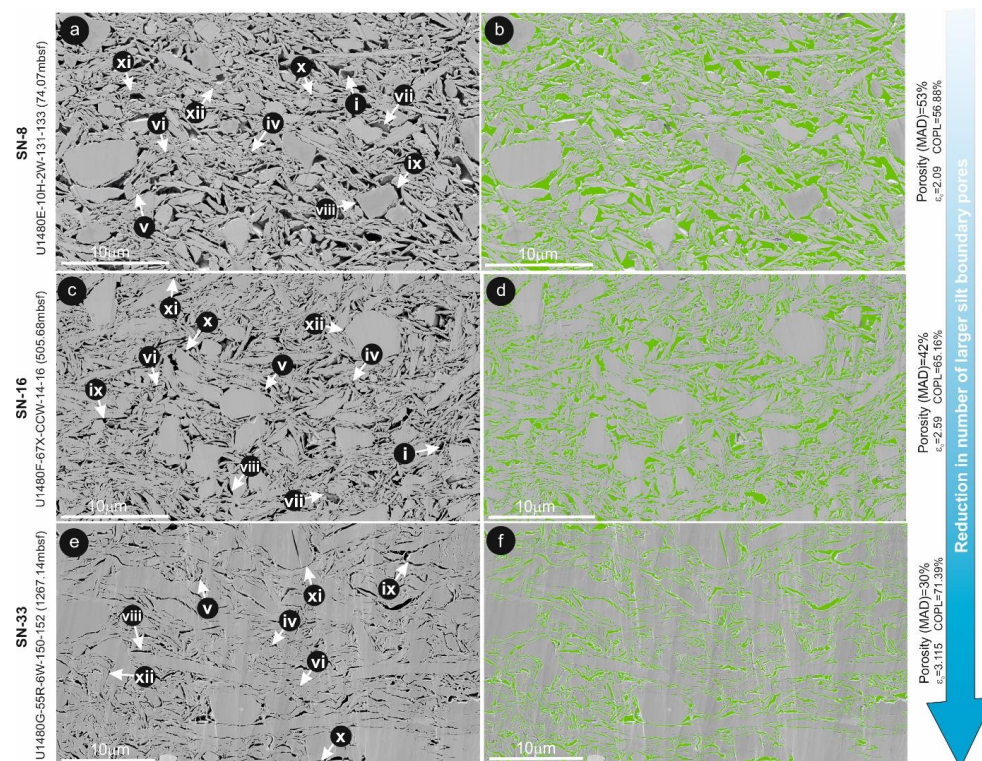
1055

1056

1057

1058

1059



1060

1061 **Fig.6:** Microstructural overview (BIB-SEM) of samples SN-8 (a and b), SN-16 (c and d), and SN-32 (e and f).
 1062 Green color represents segmented pores of the corresponding microstructure of sample. i = Equant large clay
 1063 domain pores, ii = elongated large clay domain pores, iii = Crescent-shaped large clay domain pores, iv = equant
 1064 small clay domain pores, v = Crescent-shaped small clay domain pores, vi = elongated small clay domain pores,
 1065 vii = Equant large silt-adjacent pores, viii = elongated large silt-adjacent pores, ix = Crescent-shaped large silt-
 1066 adjacent pores, x = equant small silt-adjacent pores, xi = Crescent-shaped small silt-adjacent pores, xii = elongated
 1067 small silt-adjacent pores.

1068

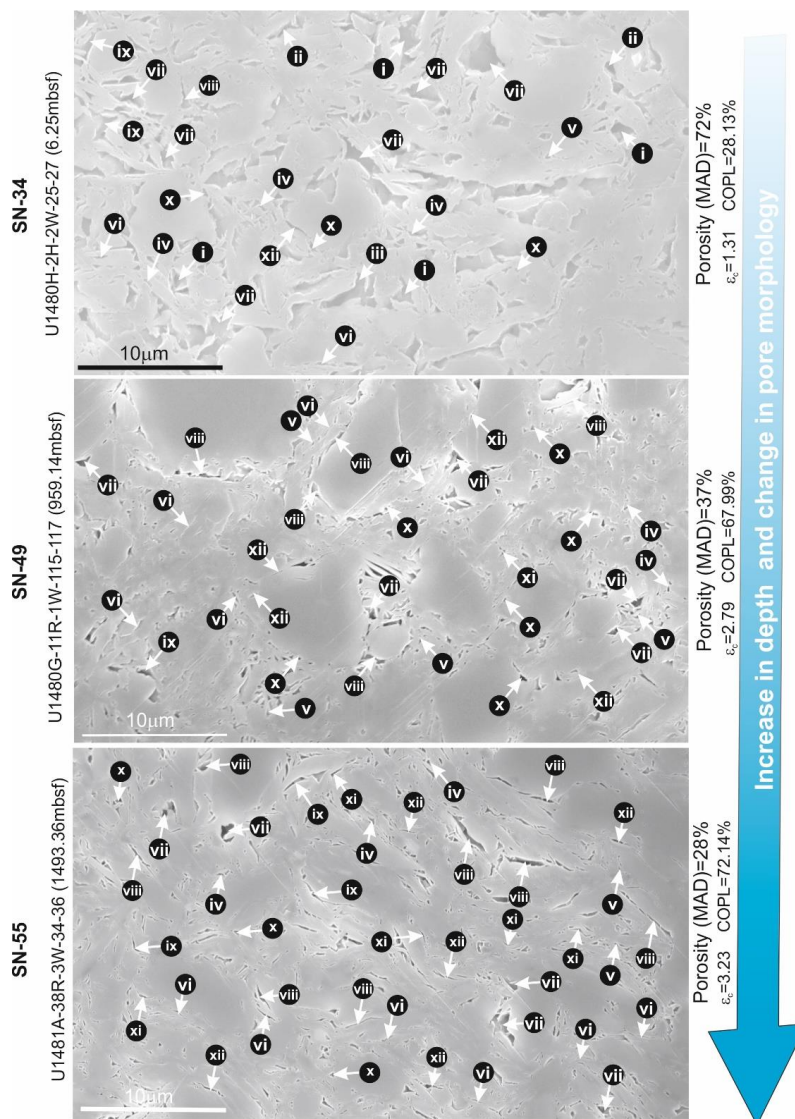
1069

1070

1071

1072

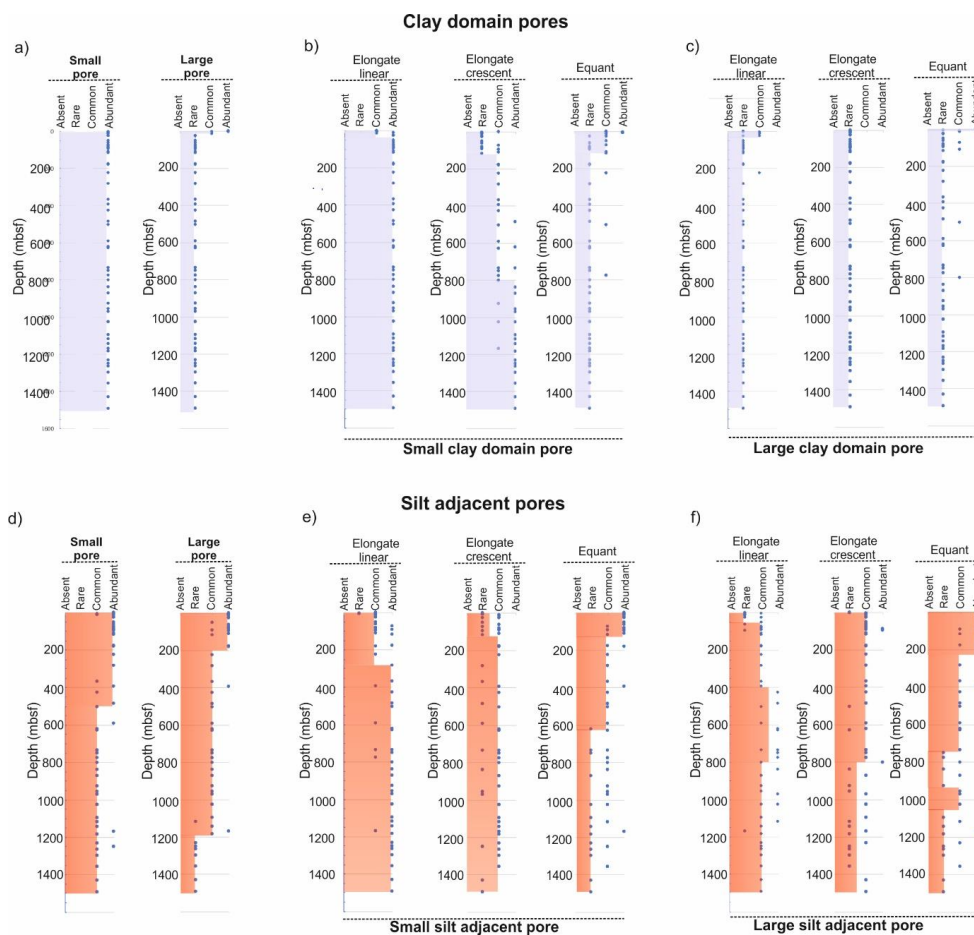
1073



1074

1075 **Fig.7:** Microstructural overview (Field Emission SEM) of samples SN-34, SN-49, and SN-55. i = Equant large
 1076 clay domain pores, ii = elongated large clay domain pores, iii = Crescent-shaped large clay domain pores, iv =
 1077 equant small clay domain pores, v = Crescent-shaped small clay domain pores, vi = elongated small clay domain
 1078 pores, vii = Equant large silt-adjacent pores, viii = elongated large silt-adjacent pores, ix = Crescent-shaped large
 1079 silt-adjacent pores, x = equant small silt-adjacent pores, xi = Crescent-shaped small silt-adjacent pores, xii =
 1080 elongated small silt-adjacent pores.

1081



1082

1083 **Fig.8:** Pore type summary for clay domain (a-c) and silt-adjacent (d-f) pore types. (a) abundance of small and large
 1084 clay domain pores; (b) and (c) depth progression of small and large clay domain pore morphologies; (d) abundance
 1085 of small and large silt-adjacent pores; (e) and (f) depth progression of small and large clay domain pore
 1086 morphologies. See text for abundance category definitions.

1087

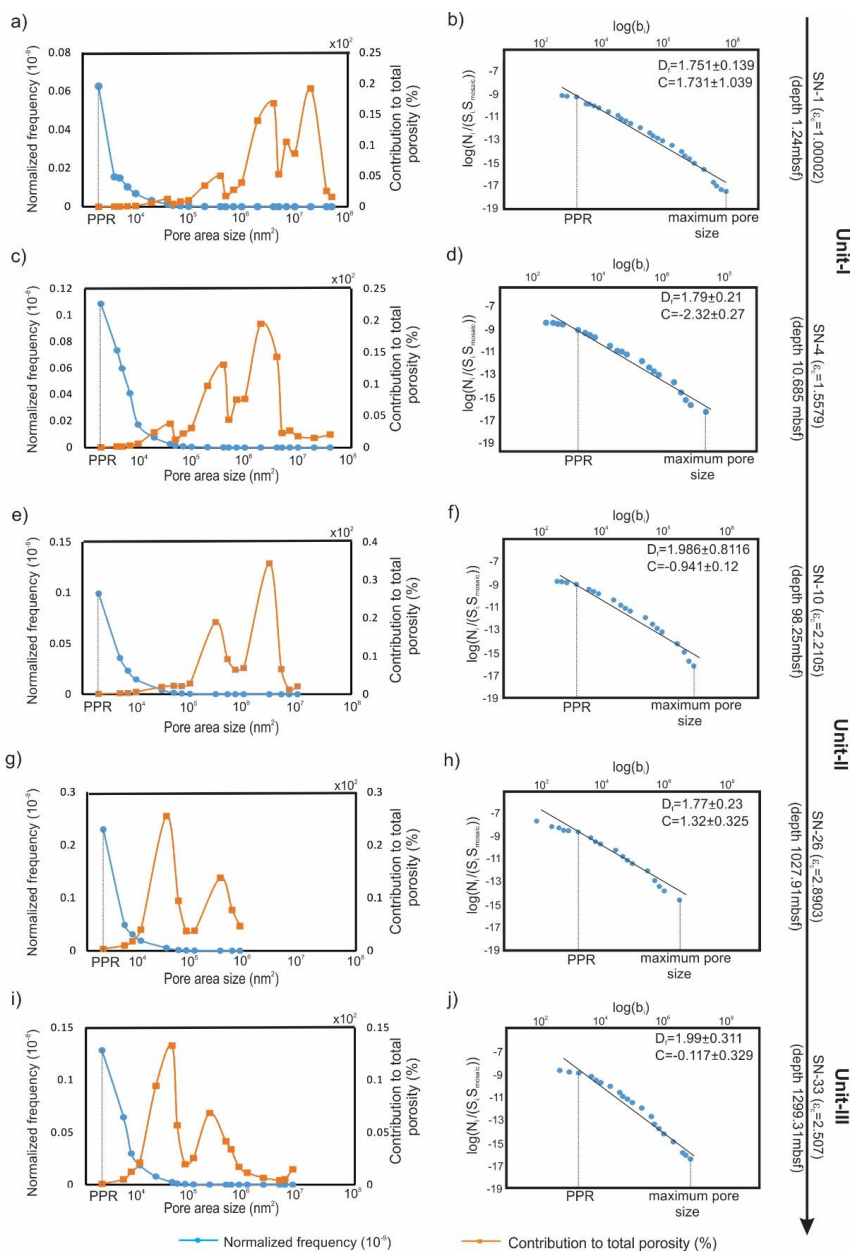
1088

1089

1090

1091

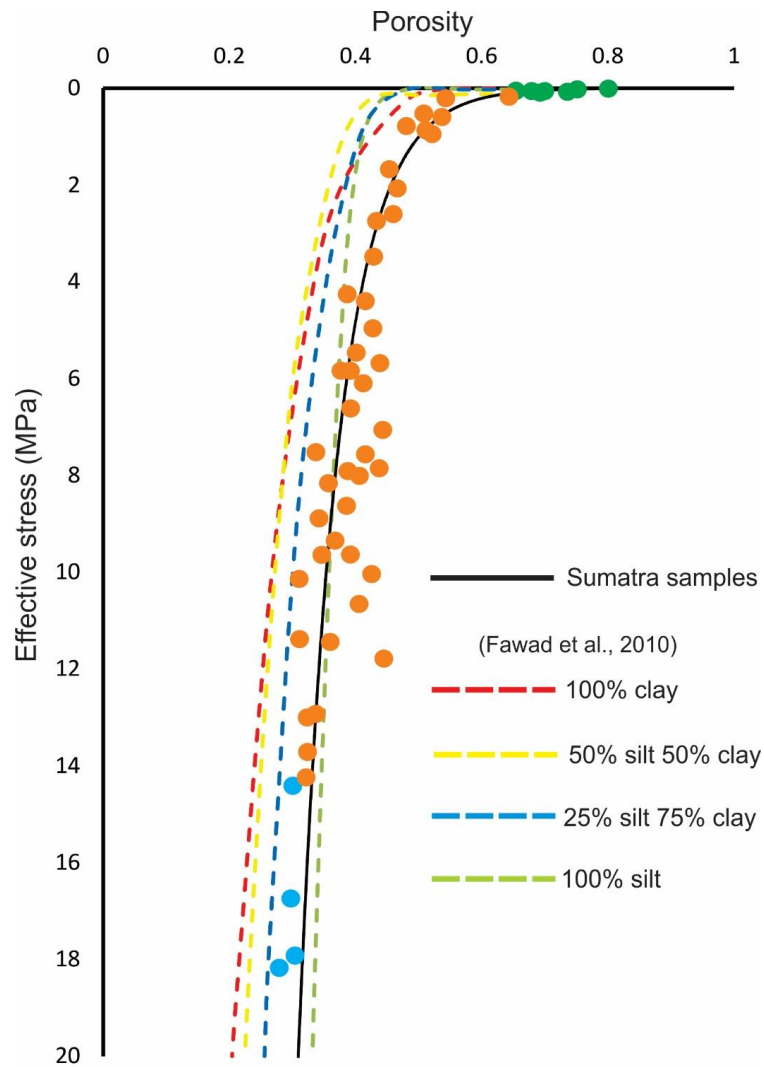
1092



1093

1094 **Fig.9:** Pore size distribution defined by pore area. Left column: normalized frequency (blue) and contribution to
 1095 total porosity (orange). Right column: pore size-frequency log-log distribution. Power-law between PPR and
 1096 maximum pore size interpreted as black line with corresponding regression parameters. Sample number, depth,
 1097 and compactional strain defined along right side of diagram

1098



1099

1100 **Fig.10:** Effective stress vs porosity for experimental mixtures of clay and silt (dashed lines; Fawad et al., 2010)
1101 compared with Sumatra data (Unit 1 = green; Unit II = orange; Unit III = blue). Solid black solid line is a best-
1102 fit data regression for Sumatra samples.

1103

1104

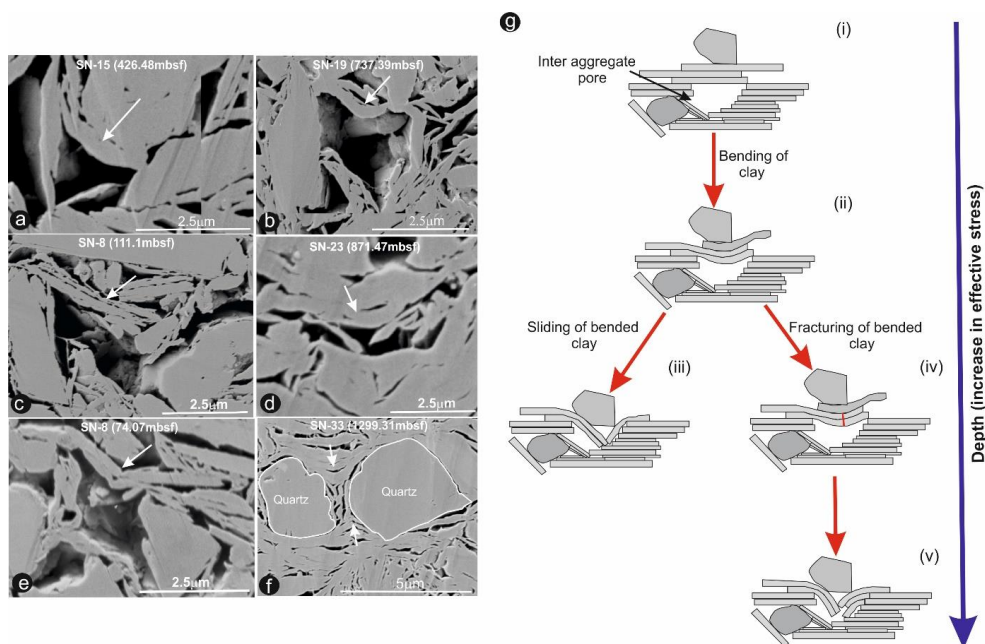
1105

1106



1107

1108



1109

1110 **Fig.11:** a-f: examples of bent clay particle on top of silt-adjacent larger pores; sample ID and depth labelled on
1111 photos. (g) Micromechanical model for collapse of large silt-adjacent pores.

1112

1113

1114

1115

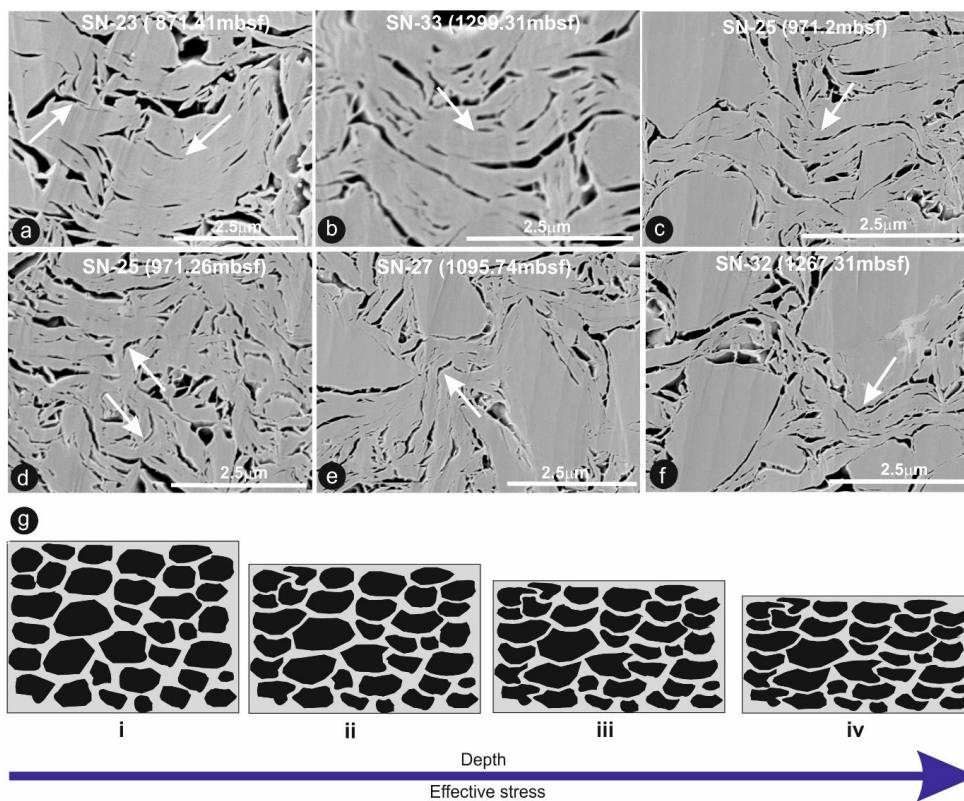
1116

1117

1118

1119

1120



1121

1122 **Fig.12:** a-f: examples of clay aggregate bending (white and black arrows). (g) Conceptual diagram tracing
1123 porosity reduction and increase in preferred alignment of the long axes of pores by bending of clay perpendicular
1124 to applied vertical stress.

1125

1126

1127

1128

1129

1130

1131

1132



1133 Table 1: Clay mineralogy in subunits of the Sumatra succession

1134	Units	Smectite (%)	Illite (%)
1135	Unit-I	33	49
1136	Unit-II	17	59
1137	Unit-III A	73	19

1139

1140

1141

1142

1143

1144

1145

1146

1147

1148

1149

1150

1151

1152

1153

1154



Table 2: Summary of pore morphology evolution with depth. Abundant = >25% pores, common = 2%-25% pores, rare = 0-2% pores, absent = not observed.

Depth (mbsf)	Sample no	Clay domain pores					Silt adjacent pores							
		Small pores (<5x10 ⁵ nm ²)	Larger pores (>5x10 ⁵ nm ²)	Small pore			Larger pore			Small pore	Larger pore			
				Elongate linear	Elongate crescent	Equant	Elongate linear	Elongate crescent	Equant					
1.24	SN-1	Abundant	Rare	Abundant	Rare	Rare	Rare	Abundant	Common	Rare	Abundant	Rare	Abundant	Abundant
5.10	SN-2	Abundant	Rare	Abundant	Rare	Rare	Rare	Abundant	Common	Rare	Abundant	Common	Common	Abundant
6.25	SN-34	Abundant	Rare	Abundant	Rare	Rare	Rare	Abundant	Common	Rare	Abundant	Rare	Abundant	Abundant
7.21	SN-35	Abundant	Rare	Abundant	Rare	Rare	Rare	Abundant	Common	Rare	Abundant	Rare	Common	Abundant
9.18	SN-3	Abundant	Rare	Abundant	Rare	Rare	Rare	Abundant	Common	Rare	Abundant	Rare	Common	Abundant
10.69	SN-4	Abundant	Rare	Abundant	Rare	Rare	Rare	Abundant	Common	Common	Abundant	Rare	Common	Abundant
14.28	SN-36	Abundant	Rare	Abundant	Rare	Rare	Rare	Abundant	Common	Common	Abundant	Rare	Common	Abundant
26.05	SN-5	Abundant	Rare	Abundant	Rare	Rare	Rare	Abundant	Common	Common	Abundant	Rare	Common	Abundant
28.00	SN-6	Abundant	Rare	Abundant	Rare	Rare	Rare	Abundant	Common	Rare	Abundant	Common	Common	Abundant
28.12	SN-37	Abundant	Rare	Abundant	Rare	Rare	Rare	Abundant	Common	Common	Abundant	Common	Common	Abundant
50.82	SN-38	Abundant	Rare	Abundant	Rare	Rare	Rare	Abundant	Common	Rare	Abundant	Common	Common	Abundant
63.24	SN-7	Abundant	Rare	Abundant	Rare	Rare	Rare	Abundant	Common	Common	Abundant	Rare	Common	Abundant
74.07	SN-8	Abundant	Rare	Abundant	Rare	Rare	Rare	Abundant	Common	Rare	Abundant	Common	Common	Abundant
83.02	SN-39	Abundant	Rare	Abundant	Rare	Common	Rare	Abundant	Common	Rare	Abundant	Common	Abundant	Abundant
87.98	SN-9	Abundant	Rare	Abundant	Rare	Rare	Rare	Abundant	Common	Rare	Abundant	Common	Common	Abundant
92.82	SN-41	Abundant	Rare	Abundant	Rare	Rare	Rare	Abundant	Common	Rare	Abundant	Common	Common	Common
98.25	SN-10	Abundant	Rare	Abundant	Rare	Rare	Rare	Abundant	Common	Rare	Abundant	Rare	Abundant	Abundant
111.10	SN-11	Abundant	Rare	Abundant	Rare	Rare	Rare	Abundant	Common	Rare	Abundant	Common	Common	Abundant
117.13	SN-40	Abundant	Rare	Abundant	Rare	Rare	Rare	Abundant	Common	Rare	Abundant	Common	Common	Common
176.50	SN-12	Abundant	Rare	Abundant	Rare	Rare	Rare	Abundant	Common	Rare	Abundant	Common	Common	Common
182.62	SN-42	Abundant	Rare	Abundant	Rare	Rare	Rare	Abundant	Common	Rare	Abundant	Common	Common	Abundant
226.70	SN-13	Abundant	Rare	Abundant	Rare	Rare	Rare	Abundant	Common	Rare	Abundant	Common	Common	Abundant
285.51	SN-43	Abundant	Rare	Abundant	Rare	Rare	Rare	Abundant	Common	Rare	Abundant	Common	Common	Common
369.19	SN-14	Abundant	Rare	Abundant	Rare	Rare	Rare	Abundant	Common	Rare	Abundant	Common	Common	Common
394.01	SN-44	Abundant	Rare	Abundant	Rare	Rare	Rare	Abundant	Common	Rare	Abundant	Common	Common	Abundant
426.68	SN-15	Abundant	Rare	Abundant	Rare	Rare	Rare	Abundant	Common	Rare	Abundant	Common	Common	Common
486.72	SN-45	Abundant	Rare	Abundant	Rare	Rare	Rare	Abundant	Common	Rare	Abundant	Common	Common	Common
505.32	SN-16	Abundant	Rare	Abundant	Rare	Rare	Rare	Abundant	Common	Rare	Abundant	Common	Common	Common
592.42	SN-17	Abundant	Rare	Abundant	Rare	Rare	Rare	Abundant	Common	Rare	Abundant	Common	Common	Common
621.2	SN-46	Abundant	Rare	Abundant	Rare	Rare	Rare	Abundant	Common	Rare	Abundant	Common	Common	Common
630.55	SN-18	Abundant	Rare	Abundant	Rare	Rare	Rare	Abundant	Common	Rare	Abundant	Common	Common	Common
737.39	SN-19	Abundant	Rare	Abundant	Rare	Rare	Rare	Abundant	Common	Rare	Abundant	Common	Common	Common
737.47	SN-47	Abundant	Rare	Abundant	Rare	Rare	Rare	Abundant	Common	Rare	Abundant	Common	Common	Common
751.16	SN-20	Abundant	Rare	Abundant	Rare	Rare	Rare	Abundant	Common	Rare	Abundant	Common	Common	Rare



Table 2: Continued

Depth (mbsf)	Sample no	Clay domain pores				Silt adjacent pores								
		Small pores (<5x10 ⁵ nm ²)	Larger pores (>5x10 ⁵ nm ²)	Small pore	Larger pore	Elongate linear	Elongate crescent	Equant	Elongate linear	Elongate crescent	Equant			
776.17	SN-21	Abundant	Rare	Abundant	Rare	Rare	Rare	Common	Common	Abundant	Common	Abundant	Common	Rare
802.55	SN-22	Abundant	Rare	Abundant	Rare	Rare	Rare	Common	Common	Abundant	Common	Abundant	Abundant	Common
841.56	SN-48	Abundant	Rare	Abundant	Rare	Rare	Rare	Common	Common	Abundant	Rare	Abundant	Rare	Rare
871.87	SN-23	Abundant	Rare	Abundant	Rare	Rare	Rare	Common	Common	Abundant	Common	Common	Common	Common
929.81	SN-24	Abundant	Rare	Abundant	Rare	Rare	Rare	Common	Common	Abundant	Common	Common	Common	Rare
959.15	SN-49	Abundant	Rare	Abundant	Rare	Rare	Rare	Common	Common	Abundant	Rare	Common	Common	Common
971.26	SN-25	Abundant	Rare	Abundant	Rare	Rare	Rare	Common	Common	Abundant	Rare	Abundant	Common	Common
1026.3	SN-50	Abundant	Rare	Abundant	Rare	Rare	Rare	Common	Common	Abundant	Common	Common	Common	Common
1027.9	SN-26	Abundant	Rare	Abundant	Rare	Rare	Rare	Common	Common	Abundant	Common	Abundant	Common	Common
1095.7	SN-27	Abundant	Rare	Abundant	Rare	Rare	Rare	Common	Common	Abundant	Common	Common	Common	Rare
1119.7	SN-28	Abundant	Rare	Abundant	Rare	Rare	Rare	Common	Rare	Abundant	Common	Common	Rare	Common
1145.9	SN-51	Abundant	Rare	Abundant	Rare	Rare	Rare	Common	Common	Abundant	Common	Common	Rare	Rare
1172.8	SN-29	Abundant	Rare	Abundant	Rare	Rare	Rare	Abundant	Abundant	Abundant	Common	Rare	Common	Abundant
1184.3	SN-30	Abundant	Rare	Abundant	Rare	Rare	Rare	Common	Common	Abundant	Common	Common	Common	Rare
1233.1	SN-31	Abundant	Rare	Abundant	Rare	Rare	Rare	Common	Rare	Abundant	Common	Common	Common	Common
1251.5	SN-52	Abundant	Rare	Abundant	Rare	Rare	Rare	Common	Rare	Abundant	Rare	Common	Rare	Rare
1267.1	SN-32	Abundant	Rare	Abundant	Rare	Rare	Rare	Common	Common	Abundant	Common	Common	Rare	Rare
1299.3	SN-33	Abundant	Rare	Abundant	Rare	Rare	Rare	Common	Rare	Abundant	Common	Common	Rare	Rare
1358.9	SN-53	Abundant	Rare	Abundant	Rare	Rare	Rare	Common	Common	Abundant	Common	Common	Rare	Common
1432.5	SN-54	Abundant	Rare	Abundant	Rare	Rare	Rare	Common	Rare	Abundant	Rare	Common	Common	Rare



Table 3: Micromechanical particle deformation process with depth

Depth	Sample	EE	EF	FF	Elongate particle bending	Cross particle fracture
1.24	SN-1	Rare	Abundant	Common	Rare	Absent
5.10	SN-2	Rare	Abundant	Common	Rare	Absent
6.25	SN-34	Rare	Common	Abundant	Rare	Absent
7.21	SN-35	Rare	Common	Abundant	Rare	Absent
9.18	SN-3	Rare	Common	Abundant	Rare	Absent
10.69	SN-4	Rare	Common	Abundant	Rare	Absent
14.28	SN-36	Rare	Common	Abundant	Rare	Absent
26.05	SN-5	Rare	Common	Abundant	Rare	Absent
28.00	SN-6	Rare	Rare	Abundant	Rare	Absent
28.12	SN-37	Rare	Common	Abundant	Rare	Rare
50.82	SN-38	Rare	Rare	Abundant	Rare	Absent
63.24	SN-7	Rare	Rare	Abundant	Rare	Absent
74.07	SN-8	Rare	Rare	Abundant	Rare	Absent
83.02	SN-39	Rare	Rare	Abundant	Rare	Absent
87.98	SN-9	Rare	Rare	Abundant	Rare	Absent
92.82	SN-41	Rare	Rare	Abundant	Rare	Absent
98.25	SN-10	Rare	Common	Abundant	Common	Absent
111.10	SN-11	Rare	Rare	Abundant	Common	Rare
117.13	SN-40	Rare	Rare	Abundant	Rare	Absent
176.50	SN-12	Rare	Rare	Abundant	Rare	Absent
182.62	SN-42	Rare	Rare	Abundant	Common	Absent
226.70	SN-13	Rare	Rare	Abundant	Common	Absent
285.51	SN-43	Rare	Rare	Abundant	Rare	Absent
369.19	SN-14	Rare	Rare	Abundant	Common	Absent
394.01	SN-44	Rare	Rare	Abundant	Common	Absent
426.68	SN-15	Rare	Rare	Abundant	Common	Absent
486.72	SN-45	Rare	Rare	Abundant	Rare	Absent
505.32	SN-16	Rare	Rare	Abundant	Common	Absent
592.42	SN-17	Rare	Rare	Abundant	Common	Absent
621.2	SN-46	Rare	Rare	Abundant	Rare	Absent
630.55	SN-18	Rare	Common	Abundant	Common	Rare
737.39	SN-19	Rare	Rare	Abundant	Rare	Rare
737.47	SN-47	Rare	Rare	Abundant	Rare	Absent
751.16	SN-20	Rare	Rare	Abundant	Common	Absent
776.17	SN-21	Rare	Rare	Abundant	Common	Absent
802.55	SN-22	Rare	Rare	Abundant	Rare	Absent
841.56	SN-48	Rare	Rare	Abundant	Common	Absent
871.87	SN-23	Rare	Rare	Abundant	Common	Rare
929.81	SN-24	Rare	Rare	Abundant	Rare	Rare
959.15	SN-49	Rare	Rare	Abundant	Rare	Rare
971.26	SN-25	Rare	Rare	Abundant	Common	Rare
1026.3	SN-50	Rare	Rare	Abundant	Common	Absent
1027.9	SN-26	Rare	Rare	Abundant	Common	Absent
1095.7	SN-27	Rare	Rare	Abundant	Common	Absent
1119.7	SN-28	Rare	Rare	Abundant	Common	Rare
1145.9	SN-51	Rare	Rare	Abundant	Rare	Absent
1172.8	SN-29	Rare	Rare	Abundant	Common	Rare
1184.3	SN-30	Rare	Rare	Abundant	Common	Absent
1233.1	SN-31	Rare	Rare	Abundant	Common	Rare
1251.5	SN-52	Rare	Rare	Abundant	Rare	Absent
1267.1	SN-32	Rare	Rare	Abundant	Abundant	Rare
1299.3	SN-33	Rare	Rare	Abundant	Abundant	Absent
1358.9	SN-53	Rare	Rare	Abundant	Common	Absent
1432.5	SN-54	Rare	Rare	Abundant	Common	Absent